

Chapter One

Introduction and Roadmap to the Thesis

Optical microcavities have now been infused into a variety of scientific arenas and have found applications in numerous technologies. The significance of their role in science and the abundance of their applications are expanding at a fast pace as higher quality factors are being achieved and novel geometries are being developed.

Quality factor (Q) is a measure of optical loss in microcavities and determines the extent of temporal confinement of optical field in these structures. Microtoroids, used throughout my thesis work, belong to the category of surface-tension-induced microcavities that have proved to provide the highest quality factors to date. Highly efficient coupling of optical power to these cavities has also been realized by extremely low-loss tapered optical fibers. Combination of ultra-high-Q microcavities and tapered fibers can hence result in minimizing optical loss in various studies, which is often the main obstacle in realizing distinct physical functionalities. The ability to attain high efficiency power transfer between two distinct waveguides is an example of the tasks that have long been tried to be addressed by optical microcavities. Chapter 2 describes my effort in attending to this long-sought goal. A universal model for the resonant-coupling efficiency is developed and confirmed by adjusting the coupling between the resonator and waveguides. Different regimes of operation are investigated, and as a result, a record waveguide-to-waveguide power transfer efficiency of 93% (0.3 dB loss) for extremely narrow bandwidth four-port couplers is achieved (57 MHz at 1550nm wavelengths). The

transfer efficiency is predicted to be even higher for narrower bandwidth filters. The substantial improvement demonstrated in this chapter, compared to all prior work on similar microcavity-type structures, elevates their performance to a level at which they could be useful for loss-sensitive quantum optical applications, which until now have not been accessible for these devices.

Chapter 2 demonstrates an almost ideal design that diminishes the optical losses to a limit where the intrinsic microcavity losses become the limiting factor in the device performance. Transcending these limits demands a precise knowledge of the sources of intrinsic optical loss in microcavities. Chapter 3 of this thesis investigates different sources of optical loss present in whispering-gallery microcavities. Scattering and absorption are generally considered the responsible loss mechanisms in limiting the quality factor of optical cavities with large enough diameters that render the whispering-gallery losses insignificant. Quality factor measurement, however, can only determine the *total* optical loss present in the device or, in other words, the sum of scattering and absorption losses. Ability to differentiate these two mechanisms, nevertheless, is instrumental in fabrication and also numerous applications of these devices. As a relevant example, fabrication of microtoroids for the first time in our laboratory was accompanied by the ambiguity as to what process limits the achievable quality factors of these cavities. Surface roughness, contaminants on the surface, or impurities in the thermally grown oxide on the silicon wafer, among many, were all equally likely to cause this limitation. Resolution on this issue could have a great impact on focusing our efforts towards efficient optimization of microtoroid fabrication.

Since the optical mode is located in the periphery of the whispering-gallery microcavities, the scattering losses are mainly due to surface roughness of these structures. Historically, therefore, the method used to determine the magnitude of scattering losses was careful theoretical estimation of the surface irregularities of microcavities and determining the surface roughness and the correlation parameters. Given the complexity of this task requiring high resolution imaging and detailed mathematical analysis of surface roughness of these microstructures, and also the inherent requirement of comparison with empirical results, I was prompted to develop an experimental technique to isolate absorption losses from those due to scattering. The circulating power in microcavities is partially absorbed and partially scattered, but only the absorbed power can generate heat and temperature rise in the structure, resulting in a nonlinearity called “thermal bistability.” This phenomenon is exploited in chapter 3 as a new tool for characterizing the relative importance of absorption and scattering losses in toroidal microcavities. An empirical realization was made during this study, of the existence of water molecules on the cavity surface, the optical absorption of which is the dominant loss mechanism under certain conditions. Based on this result, thermal nonlinearity of microtoroids was used to reveal the role of surface contaminants in absorption losses, and hence to study the interaction of microtoroids with their ambient environment. Prospects of this work could be beneficial in sensing applications, an example of which is illustrated in detail in chapter 3.

Extremely low intrinsic losses in ultra-high-Q optical microcavities (e.g., microspheres and microtoroids) make them also ideally suited for observing nonlinear optical effects with extremely low (sub-microwatt) threshold powers. The combination of

high circulating power made possible by high quality factor and strong confinement of this power within mode volumes of the order of hundreds of μm^3 lead to inter-cavity circulating intensities, which are sufficient to unveil nonlinear phenomena even in materials like silica that are weakly nonlinear. Thermal nonlinearity, for instance, is not the only effect contributing to the bistability effect observed in experiments in chapter 3. Optical Kerr effect or intensity-dependent refractive index phenomenon leads to optical bistability in a similar way as do thermal nonlinearities. The observation of this effect, however, is problematic as it is accompanied by relatively larger thermal nonlinear effects. In an attempt towards observation of this nonlinearity in micro-cavities, evidence is found for Kerr bistability by immersing microspheres in a superfluid helium bath at 2K. This cryogenic setup greatly reduces the sensitivity of WGM resonances to temperature and allows the Kerr effect to be dominant and hence observable. In chapter 4, however, an innovative method for observing the optical Kerr effect in microcavities at room temperature and in presence of the dominant thermal nonlinearities is proposed and experimentally verified. The technique discriminates against the much larger and typically dominant thermal component of nonlinearity by using its relatively slow frequency response compared to the almost instantaneous Kerr effect. Measurement of the Kerr coefficient (n_2), or equivalently third-order nonlinear susceptibility of the cavity material ($\chi^{(3)}$), is demonstrated for the case of a silica microcavity. With this approach useful information about the characteristic thermal response time in microresonators can also be acquired.

Whispering-gallery microresonators have historically been perceived as structures that could efficiently confine optical energies. This is due to their exceedingly low losses

at optical frequencies. In the final years of my Ph. D. studies, I had the opportunity to explore the quality of these structures in a starkly different frequency range. Optical microcavities like any other structure have mechanical eigenmodes or resonant modes of vibration. The same way that optical Q factor describes the temporal energy confinement in optical frequencies, a quality factor can be associated to each one of these mechanical eigenmodes, representing the efficiency of energy storage at mechanical frequencies. The micron size of these structures results in vibrations at radio frequencies, about seven orders of magnitude apart from the optical frequencies. Mechanical quality factors of toroidal microcavities at their eigenfrequencies of vibration (1-100 MHz in devices studied in this thesis) are measured in chapter 5. Q factors in excess of 5,000 are reported in this chapter, revealing a heretofore unknown potential of these structures in storing energy at frequencies remarkably distant from their optical resonant modes. This realization stimulates a curiosity as to whether these two resonators, an optical one resonating at 100 THz and a mechanical one resonating at tens of MHz frequencies now both present in the same device, could potentially be coupled to each other.

Chapter 5 describes how radiation-pressure or the force due to impact of photons could result in exceptionally strong coupling between these two resonators. The discovered optomechanical coupling present in toroid microcavities is shown to reach such a high level that could initiate regenerative mechanical oscillations of the cavity structure with only microwatts of optical threshold power. This is the first demonstration of radiation-pressure-induced mechanical oscillations in any type of optomechanical system. Chapter 5 presents a detailed theoretical and experimental analysis of this effect in ultra-high-Q microtoroids. Embodied within a microscale, chip-based device, this

mechanism can both benefit research into macroscale quantum mechanical phenomena and improve the understanding of the mechanism within the context of Laser interferometer gravitational-wave observatory (LIGO). It also suggests that new technologies are possible that will leverage the phenomenon within photonics.

Chapter 6 provides a brief summary of the presented material in this thesis and its significance and prospects for different scientific communities and technological applications.

Chapter Two

Ultra-Low-Loss, High-Q, Four-Port Resonant Couplers

2-1 Introduction

Minimizing optical loss is of crucial importance in various studies, as it is often the main obstacle in realizing distinct physical functionalities. This is true in quantum optical applications of microcavities where parasitic loss can both inhibit the generation of quantum states and interfere with intended coupling to a transport medium such as optical fiber [1-8]. Also, in photonic applications of these devices [9-12], the ability to attain high-efficiency power transfer between two distinct waveguides is of great interest. The ability to attain coupling coefficients between the resonator and waveguides that are greater than the intrinsic roundtrip loss of the cavity (usually called the overcoupled regime) is fundamental to achieve high waveguide-to-waveguide resonant power-transfer efficiency. High waveguide coupling efficiency and high intrinsic quality factor (Q) are hence essential in almost all applications of waveguide-coupled resonator systems. Such characteristics ensure that overall quality factor of the system can be dominated by the intentional control of waveguide loading (coupling into and out-from the resonator) as opposed to parasitic mechanisms that include intrinsic losses of the cavity and scattering losses at the waveguide-resonator junctions.

In this chapter an all-optical four-port resonant coupler (add-drop geometry) is demonstrated. Ultra-high-Q ($>10^8$) toroidal microcavities [13] and tapered optical fibers

are the building blocks of this filter configuration. A new realm of performance is enabled for operation of these devices, combining the ultra-high-quality-factor (UHQ) microresonators ($Q > 10^8$) [7,8,13] and the ability to provide high efficiency coupling to these cavities by use of low-loss tapered fiber waveguides [14].

A model for the resonant-coupling efficiency and quality factor variation versus waveguide loading is developed and confirmed by adjusting the coupling between the resonator and waveguides. Different regimes of operation are investigated and, as a result, waveguide-to-waveguide power transfer efficiency of 93% (0.3 dB loss) and nonresonant insertion loss of 0.02% (< 0.001 dB) for narrow bandwidth (57 MHz at 1550nm wavelengths) four-port couplers are achieved. The transfer efficiency is predicted to be even higher for narrower bandwidth filters. This represents a substantial improvement compared to all prior work on similar microcavity-type structures, elevating their performance to a level at which they could be useful for loss-sensitive quantum optical applications that until now have not been accessible for four-port resonant couplers. The combination of low loss, fiber compatibility, and wafer-scale design would be suitable for a variety of applications ranging from quantum optics to photonic networks.

2-2 Add-Drop Geometry and Power Transfer Efficiency

Figure 2.1 depicts the device geometry including a UHQ microtoroid resonator evanescently side-coupled to a pair of tapered optical fibers. In this configuration where a whispering-gallery mode enables resonant power transfer between two distinct waveguides, the microcavity acts as a frequency selective coupler. Resonant optical power (λ_2 in Figure 2.1) launched into port 1 is transferred to port 4 via the microtoroid, while nonresonant waves are largely unaffected upon transmission beyond the resonator-waveguide junction. This system (symmetric or asymmetric geometry add/drop [15]) can be studied using a simple model based on the assumption of weak coupling between the resonator and waveguides, which is valid in the current work. Weak coupling allows the separation of individual contributions to the cavity field decay time. A quality factor can be assigned to each dissipation process where the total quality factor takes the following compact form:

$$\frac{1}{Q_{total}} = \frac{1}{Q_0} + \frac{1}{Q_{bus}} + \frac{1}{Q_{drop}} \quad (2.1)$$

Q_{bus} and Q_{drop} are quality factors associated with coupling to bus (input) and drop (output) waveguides, respectively. The overall quality factor of the system (Q_{total}) determines the filter bandwidth and is lower than the intrinsic Q of the cavity (Q_0), due to the intentionally introduced couplings at the waveguide-resonator junctions.

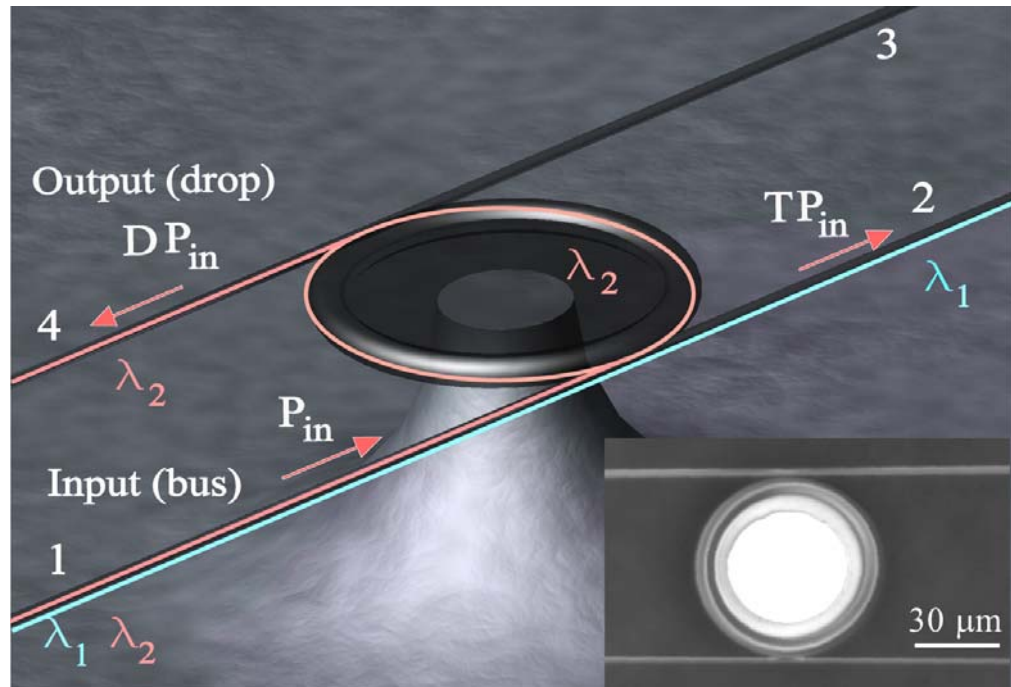


Figure 2.1: Illustration showing a microtoroid four-port filter (add/drop geometry). Wavelength λ_2 in the bus waveguide is resonant with a whispering gallery mode of the resonator and subsequently couples to the drop waveguide. Nonresonant launched power (λ_1) is transmitted past the resonator-waveguide junction. Inset is a top view photomicrograph of a microtoroid coupled to two tapered optical fibers.

The following relationship exists between the transmitted and dropped power:

$$\left[1 + \frac{Q_{drop}}{Q_0}\right]D = 1 - T \quad (2.2)$$

where T and D are the transmitted and coupled (dropped) powers normalized to the incident signal power (see Figure 2.1). Assuming a fixed coupling between the resonator and the drop waveguide (fixed Q_{drop}), the dropped power to port 4 and the transmitted power to port 2 lie on a straight line, as coupling to the bus waveguide (Q_{bus}) varies. At the critical coupling point ($T=0$) [16,17], the drop efficiency reaches its maximum value:

$$D_{max} = 1 - \frac{2Q_{total}}{Q_0} \quad (2.3)$$

The important role of high intrinsic Q cavities (high Q_0) in obtaining high-power transfer efficiency is apparent in this expression. The condition of criticality, $Q_{bus}^{-1} = Q_{drop}^{-1} + Q_0^{-1}$, assures that coupling to the resonator from the input waveguide compensates both for the intrinsic loss of the cavity and the power coupling to the drop waveguide. It also ensures high transmission extinction of the resonant signal in the input waveguide.

The sources of deviation from unity efficiency include the degree to which the resonator is non-critically coupled ($T>0$), the high, but nonetheless finite intrinsic Q factor of the resonator, and the parasitic losses at the resonator-waveguide junction, which include both scattering losses and coupling to the undesired modes of the tapered fiber [14]. As will be discussed later in the chapter, the latter losses, which can be effectively lumped in to the Q_0 of the coupled resonator, are negligible in this work. Also, throughput extinctions above 30 dB ($T < 0.001$) are achieved, which rules out the non-

critical coupling as a significant source of power transfer inefficiency. Therefore in this work the efficiency is solely limited by the finite Q of the cavities.

2-3 Experimental Results

To confirm the theoretical analysis, microtoroids of various sizes and quality factors were fabricated according to the previously reported microtoroid fabrication process [13]. Low loss (<0.3 dB) fiber-tapers, serving as input and drop waveguides, were simultaneously made by the technique of continuous flame-heating and stretching of two standard single-mode fibers. The device presented in this chapter is a microtoroid of principal diameter 65 μm and minor diameter of approximately 6 μm . Fiber tapers used in the measurement had waist diameters of approximately 1 μm and 1.7 μm , for bus and drop waveguides respectively. The chip containing the microtoroid was held on a platform that could be manipulated relative to the waveguides using a 10 nm step-resolution piezoelectric stage. To fulfill the assumption of constant coupling to the drop channel (fixed Q_{drop}), the fiber taper used for the drop waveguide was held in contact with the resonator. The other waveguide was manipulated using a probe controlled by a high-resolution micropositioner. A single mode, tunable, external cavity laser, emitting in the 1550 nm band, was used to excite the whispering gallery modes of the microtoroid. Transmission and drop powers were simultaneously monitored using two (125 MHz) photodiode detectors, as the laser frequency was slowly (<10 Hz) scanned over about 50 GHz using a function generator. Before discussing the experimental results it should be noted that in the present work the power-transfer efficiency has reached such a high level that uncertainties in power measurements associated with losses external to the device such as

splice losses are vastly larger than the resonator-based transfer loss itself. In this regard, external losses incurred by mode conversion from a single mode fiber to the thin waveguides at the resonator coupling region can be excluded in the device efficiency measurements. This is done by using port 1 and port 2 as input ports for the device in separate measurements and subtracting off the individual losses of the bus and drop fiber taper mode converters (about 0.15 dB per converter). Using this technique accuracy in transfer loss measurements of about 0.1 dB ($\sim 3\%$) can be achieved. Since precision of efficiency measurements is limited to this level, in order to verify our theoretical predictions we opt to measure the efficiency in more weakly loaded toroid filters having correspondingly higher Q_{total} factors and hence lower transfer efficiencies (see equation 2.3). To this end, waveguides with larger waist diameters can be used to limit the extent of the evanescent field and thereby reduce the waveguide-resonator coupling.

Coupling to the resonator by each fiber taper, acting alone was first examined. Resonator line-width measurements using a single waveguide in the highly undercoupled regime ($Q_{total} \cong Q_0$) revealed a 3 dB bandwidth of about 1.9 MHz at the resonant wavelength of 1565 nm, which translates to an intrinsic resonator quality factor of 1×10^8 .

Figure 2.2 shows optical transmission vs. air gap using the input (bus) taper. Over-coupled transmission as high as 96% was observed demonstrating the high ideality of the junction. The efficiency of coupling between the fundamental mode of the tapered fiber and the resonant mode of microtoroid can be estimated using the transformation introduced in reference 11:

$$K = \frac{1 \pm \sqrt{T}}{1 \mp \sqrt{T}} \quad (2.4)$$

In this expression, T is the transmission beyond the taper-resonator junction, and K is the ratio of desired waveguide mode coupling to total parasitic losses of the system (intrinsic round-trip loss of the cavity, and parasitic coupling losses at the junction). The upper and lower signs are taken for overcoupled and undercoupled regimes, respectively. Non-ideality arises from parasitic losses, i.e., coupling of the resonator mode to either the radiation modes or the higher-order modes of the fiber-taper-waveguide, which subsequently are radiated or coupled to cladding modes upon transition to the single-mode fiber. Ideality of the coupling junction can be deduced by plotting K vs. gap distances on a logarithmic scale. In cases where the parasitic couplings are masked by the intrinsic resonator loss, this plot will be a single slope line and a lower bound on the ideality can be inferred by measuring K values at the smallest possible separations. The inset in Figure 2.2 is such a plot for the device under study. K values well above 100 place a lower bound on junction ideality of better than 99% in the overcoupled regime ($Q_{bus} < Q_0$) meaning that less than 1% of power is coupled to undesired modes of the tapered fiber. This clearly demonstrates that parasitic losses at the junction are minimal and can be ignored (at least in the presented experiments) compared to the intrinsic losses of the cavity.

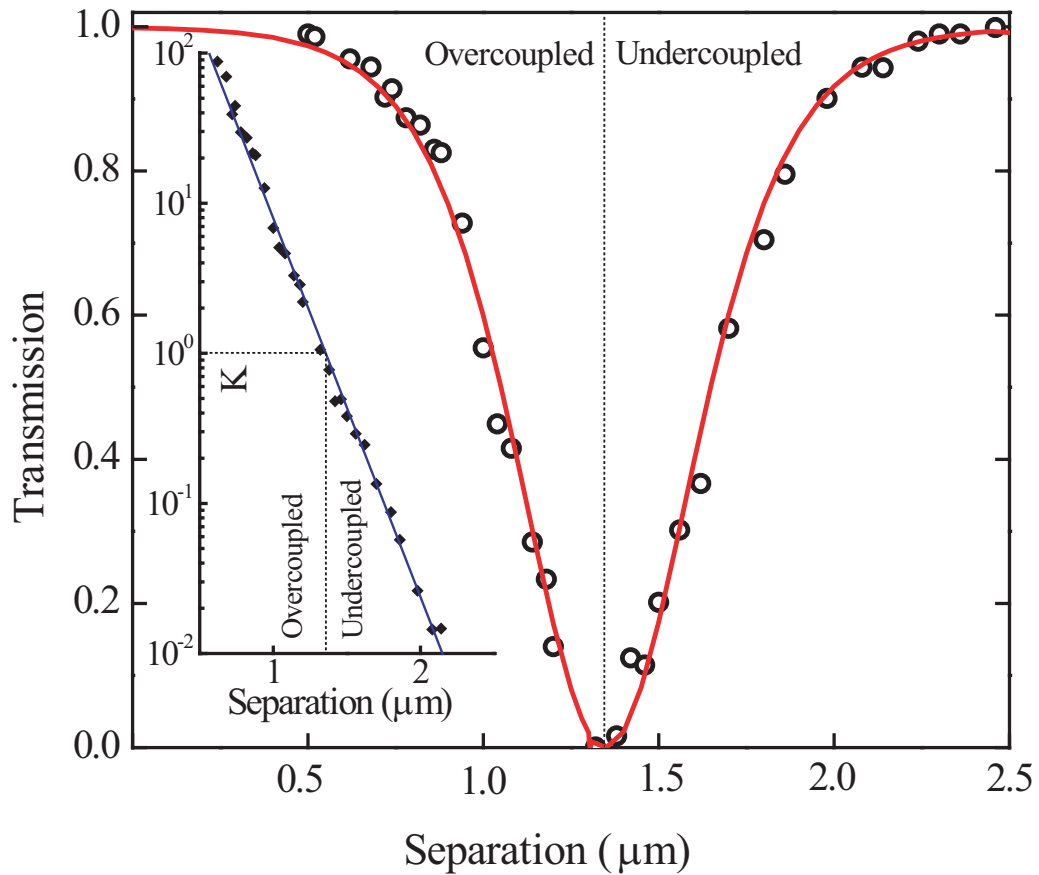


Figure 2.2: Transmission plotted versus taper-toroid separation. Overcoupling as high as 96% is measured. The inset is a plot of K versus position and illustrates the quality of junction. A lower bound of 99% on Ideality in the overcoupled regime can be inferred from this plot. The dotted line marks the critical coupling point at 1.3 μm gap distance.

Figure 2.3 shows the drop efficiency D (the fraction of power at the first waveguide redirected to the second waveguide), measured for different loading regimes and plotted versus the ratio of the intrinsic Q to the loaded quality factor of the system. Data were measured as the gap between input waveguide and resonator was varied. As noted earlier, the drop waveguide coupling is fixed during these measurements. As an aside, note that the total quality factor is reduced by a factor of 15 (labeled in Figure 2.3) upon attachment of the drop waveguide to the resonator. The Q factor at the critical coupling point is a factor of 30 lower than the intrinsic Q ($=10^8$), corresponding to a filter bandwidth of 57 MHz. From equation (2.3), the factor of 30 yields a maximum theoretical drop efficiency of 93.3% (0.3 dB loss) in good agreement with the measured values in Figure 2.3. The inset in Figure 2.3 is a plot of the measured transmission versus the drop power and confirms the predicted linear relationship. This way of plotting the data results in a more reliable estimate of the maximum drop efficiency, which is $(94 \pm 3)\%$ for this device. This is the best efficiency ever reported for a four-port microcavity-type resonant coupler. It also agrees well with the expected theoretical value of 93.3%. The transmission data are obtained by normalizing the on-resonance transmission to its value with the resonator far from the waveguides. The nonresonant insertion loss in the bus channel was measured to be less than 0.02% during the experiment. This loss, as noted earlier, is due to scattering of the evanescent field at the waveguide-resonator junction and is measured by comparing the off-resonance transmission in port 2, when the device is working as an add/drop, to the same transmission but when the resonator is far from the bus waveguide (infinite gap). As

such, the measurement of insertion loss yields a higher level of accuracy and precision than is possible for measurement of the drop efficiency.

The small deviation from the ideal case of infinite intrinsic Q can be observed in the inset of Figure 2.3 (see the dashed line). This deviation, a direct consequence of energy conservation, is due to the power dissipation in the cavity due to finite intrinsic losses. Note that in the theoretical model, all parasitic losses have been lumped into Q_0 . Therefore the excellent agreement between the measured values for the efficiency and the theoretical predictions, which assume all the parasitic losses come from the intrinsic loss of the cavity, are further evidence of low loss at the waveguide-resonator junctions. Figure 2.3 also shows that the bus waveguide can induce at least a factor of 10^3 decrease in quality factor relative to that of the original resonator ($Q_0 = 10^3 Q_{bus}$). Were the drop waveguide designed to produce this level of coupling, an exceedingly high drop efficiency of 99.9% would result with an overall loaded Q factor of 5×10^4 or a filter bandwidth of about 4 GHz. Higher bandwidths in this range are of interest in telecommunication applications of these devices [18-20].

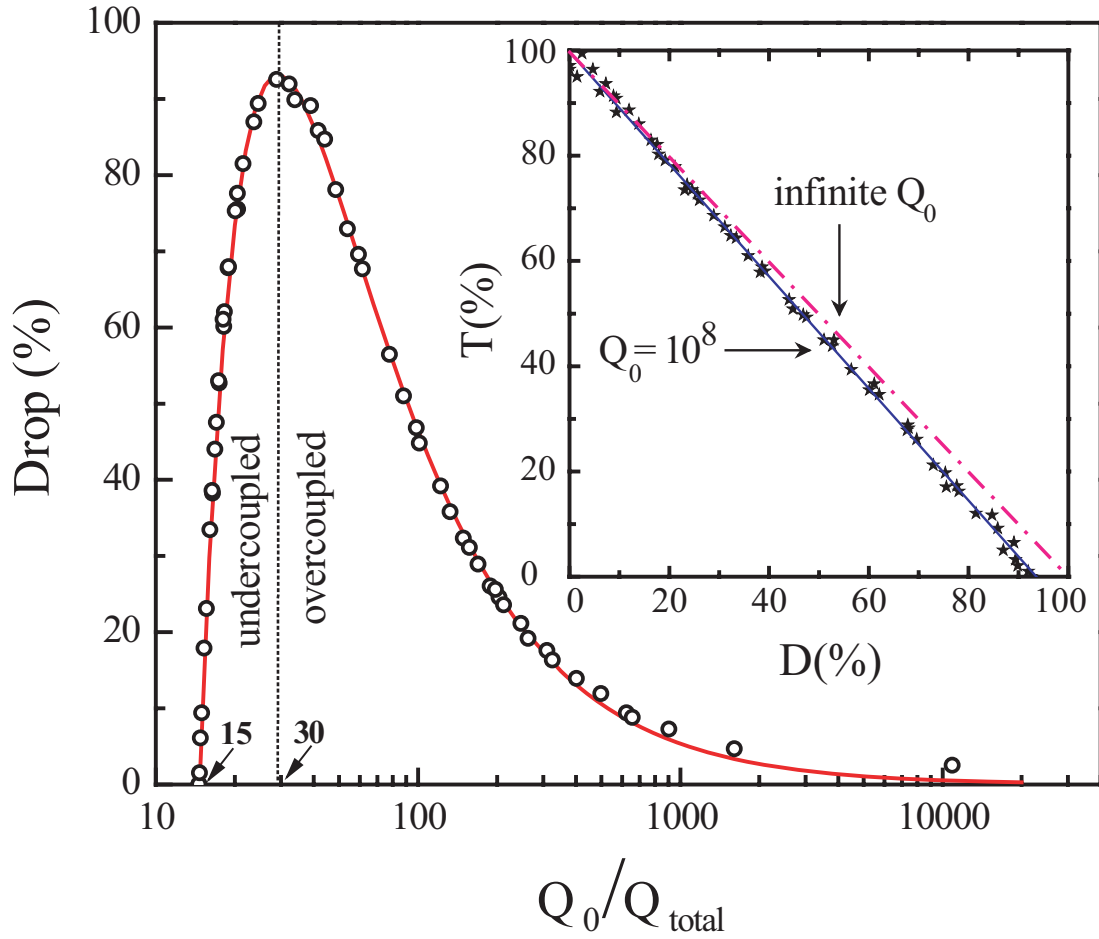


Figure 2.3: Transferred power to the drop waveguide (D) versus the inverse-loaded Q of the system. The data shows a factor of 15 reduction in Q factor upon attachment of the drop taper to the resonator. At the critical coupling point ($Q_0/Q_{total} = 30$), 93% of the input power is transferred to the drop port and throughput transmission vanishes. The theoretical drop efficiency is given by the solid line. The inset is a plot of T and D measured for the same coupling levels in the main Figure and verifying their linear relationship. The solid curve is the theoretical curve, and the dashed curve gives the ideal case of infinite intrinsic Q .

Figure 2.4 shows transmission and drop spectra measured for a device designed to operate in the higher bandwidth regime. The filter shape is Lorentzian and the bus waveguide extinction is a record 33 dB. Note that the FWHM of the drop and transmission spectra almost coincide due to almost negligible amount of loss in power transfer process.

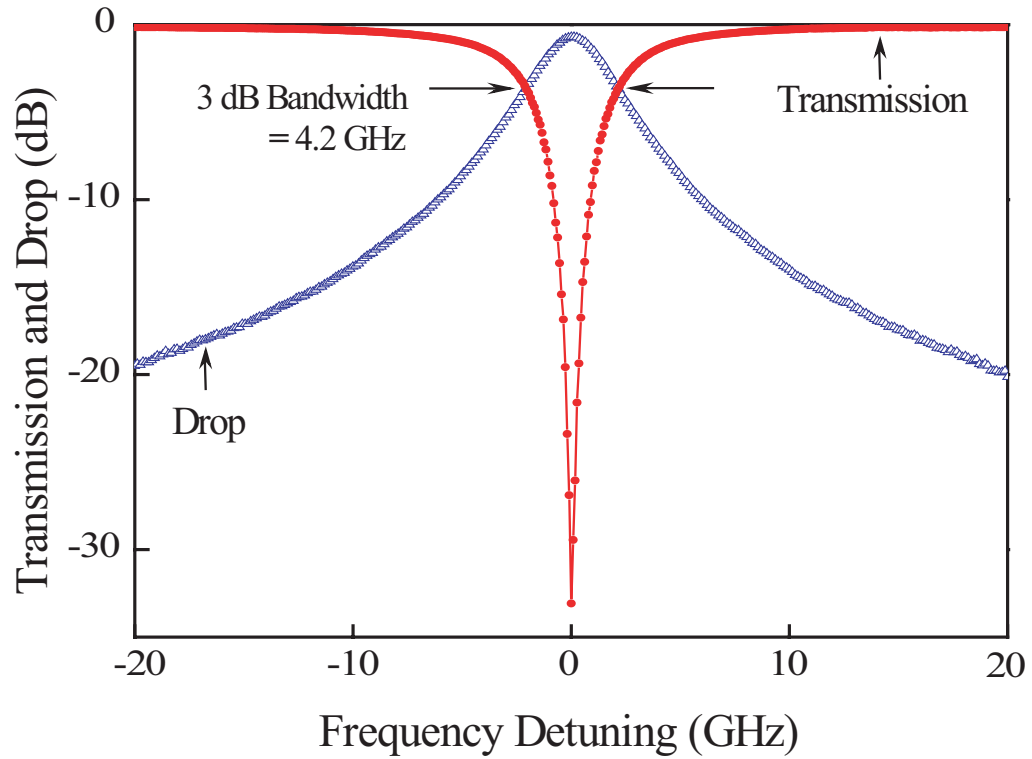


Figure 2.4: Drop port (triangles) and throughput port (circles) spectra measured for a four-port resonant coupler with 4.2 GHz bandwidth. Extinction of 33 dB in input channel occurs at the resonant wavelength of 1540 nm.

To characterize the performance of this filter for telecommunication purposes, using an external Mach-Zehnder modulator, the laser power launched into port one was modulated with $2^{31} - 1$ PRBS data, and the quality of the received signal was monitored at the drop port. Figure 2.5 shows the bit error rate (BER) curves obtained from dropped data at 10 Gbit/s. Also plotted is the so-called back-to-back data obtained by removal of the filter. The 0.7 dB power penalty, without any sign of error floor, is attributed to the finite pass band of the filter response, resulting in cut off of the high frequency components of the signal.

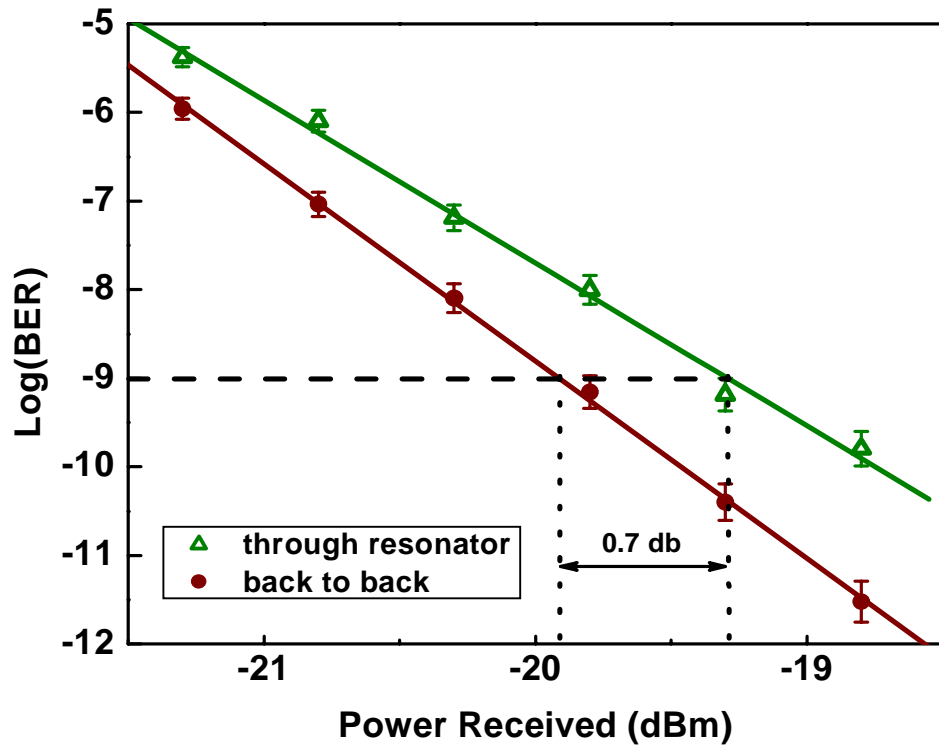


Figure 2.5: Back-to-back (circles) and through-the-resonator (triangles) BER measurements taken using an all-optical four-port coupler device at 10 Gbit/s data rates. There is a 0.7 dB power penalty when the add-drop is used owing to its finite bandwidth.

2-4 Conclusions

The results presented in this chapter demonstrate the ability of taper-coupled ultra-high-Q toroid microcavities to reach exceedingly high power-transfer efficiencies in add-drop filter applications. This can be of great interest in the study of processes requiring very low loss. As an example, losses are one of the main impediments in realizing long-distance quantum communication networks, as they tend to destroy the entanglement of quantum states and ultimately decrease the communication fidelity [21]. Also the ability to filter out broad-band noise while maintaining the signal amplitude (low insertion loss) is highly desirable in radio-frequency photonics [22] or sensitive power detection applications (e.g., single photon experiments). The latter application requires high-finesse cavities to achieve strong out-of-band noise rejection. A free spectral range of about 8 nm and loaded Q of 3.3 million implies a finesse in excess of 10^4 for the device studied here. On the other hand, due to the extremely low intrinsic loss of cavities in these devices, the quality factor of the system is almost entirely determined by coupling to waveguides. Therefore, a remarkable operational dynamical range (both bandwidth and power-transfer ratio) is attainable by controlling the coupling between resonator and individual waveguides. Finally, the excellent agreement of the experimental results with theoretical predictions suggests that this method allows the realization of resonant couplers with negligible losses. Indeed, the selection of filter design in the present study was intended to produce a measurable loss within the accuracy of our experimental equipment for purposes of comparison to the model.

2-5 Bibliography

- [1] H. J. Kimble. Strong interactions of single atom and photons in cavity QED. *Physica Scripta*, T76: 127-137, 1998.
- [2] S. Haroche. Entanglement, mesoscopic superposition and decoherence studies with atoms and photons in a cavity. *Physica Scripta*, T76: 159-164, 1998.
- [3] A. Kiraz *et al.* cavity-quantum electrodynamics using a single InAs quantum dot in a microdisk structure. *Applied Physics Letters*, 78(25): 3932-3934, 2001.
- [4] J. I. Cirac, P. Zoller, H. J. Kimble, and H. Mabuchi. Quantum state transfer and entanglement distribution among distant nodes in a quantum network. *Physical Review Letters*, 78(16): 3221-3224, 1997.
- [5] J. M. Gerard, *et al.* InAs quantum boxes in GaAs/AlAs pillar microcavities: from spectroscopic investigations to spontaneous emission control. *Physica E*, 2(1-4): 804-808, 1998.
- [6] E. Waks *et al.* Secure communication: Quantum cryptography with a photon turnstile. *Nature*, 420(6917): 762-762, 2002.
- [7] D. W. Vernooy, A. Furusawa, N. P. Georgiades, V. S. Ilchenko, and H. J. Kimble. Cavity QED with high-Q whispering gallery modes. *Physical Review A*, 57(4): R2293-R2296, 1998.
- [8] V. B. Braginsky, M. L. Gorodetsky, and V. S. Ilchenko. Quality-factor and nonlinear properties of optical whispering-gallery modes. *Physics Letters A*, vol. 137(7-8): 393-397, 1989.

- [9] B. E. Little, S. T. Chu, W. Pan, D. Ripin, T. Kaneko, Y. Kokubun, and E. Ippen. Vertically coupled glass microring resonator channel dropping filters. *IEEE Photonics Technology Letters*, 11(2): 215-217, 1999.
- [10] S. Suzuki, Y. Hatakeyama, Y. Kokubun, and S. T. Chu. Precise control of wavelength channel spacing of microring resonator add-drop filter array. *Journal of Lightwave Technology*, 20(4): 745-750, 2002.
- [11] K. Djordjev, S. J. Choi, and P. D. Dapkus. Vertically coupled InP microdisk switching devices with electroabsorptive active regions. *IEEE Photonics Technology Letters*, 14(8): 1115-1117, 2002.
- [12] P. Rabiei, W. H. Steier, C. Zhang, and L. R. Dalton. Polymer micro-ring filters and modulators. *Journal of Lightwave Technology*, 20(11): 1968-1975, 2002.
- [13] D. K. Armani, T. J. Kippenberg, S. M. Spillane, and K. J. Vahala. Ultra-high-Q toroid microcavity on a chip. *Nature*, 421(6926): 925-928, 2003.
- [14] S. M. Spillane, T. J. Kippenberg, O. J. Painter, and K. J. Vahala. Ideality in a fiber-taper-coupled microresonator system for application to cavity quantum electrodynamics. *Physical Review Letters*, 91(4): art. no. 043902, 2003.
- [15] A. Vorckel, M. Monster, W. Henschel, P. H. Bolivar, and H. Kurz. *IEEE Photonics Technology Letters*, 15(7): 921-923, 2003.
- [16] M. Cai, O. Painter and K. J. Vahala. Observation of critical coupling in a fiber taper to silica-microsphere whispering gallery mode system. *Physical Review Letters*, 85(1): 74-77, 2000.
- [17] A. Yariv. Critical coupling and its control in optical waveguide-ring resonator systems. *IEEE Photonics Technology Letters*, 14(4): 483-485, 2002.

- [18] B. J. Offrein *et al.* Resonator coupler-based tunable add-after-drop filter in Silicon-nitride technology for WDM networks. *IEEE Journal of Selected Topics in Quantum Electronics*, 5(5): 1400-1406, 1999.
- [19] R. Grover *et al.* Vertically coupled GaInAsP-InP microring resonators. *Optics Letters*, 26(8): 506-508, 2001.
- [20] B. E. Little, S. T. Chu, H. A. Haus, J. Foresi, and J. P. Laine. Micro-ring resonator channel add-dropping filters. *Journal of Lightwave Technology*, 15(6): 998-1005, 1997.
- [21] S. J. van Enk, J. I. Cirac, P. Zoller. Ideal quantum communication over noisy channels: A quantum optical implementation. *Physical Review Letters*, 78 (22): 4293-4296, 1997.
- [22] X. S. Yao and L. Maleki. Optoelectronic microwave oscillator. *Journal of Optical Society of America B*, 13(8): 1725-1735, 1995.

Chapter Three

Loss Characterization in Microcavities Using the Thermal Bistability Effect

3-1 Introduction

At sufficiently high quality factors (Q), whispering gallery mode microresonators can enter a regime where minute injected optical powers can result in large thermal nonlinearities [1-2]. The circulating intensity in these cavities, greatly enhanced due to their high quality factors and small mode volumes, is partially absorbed, and the generated heat can produce thermal bistability [3]. In this chapter we exploit this phenomenon as a new tool for characterizing distinct optical loss mechanisms responsible for limiting the quality factor of high- Q microresonators [4]. A powerful method is demonstrated, based on the thermal bistability effect, to characterize the relative importance of absorption and scattering losses in toroidal microcavities. Empirical results on thermal nonlinearity of these structures have been used to study the interaction of microtoroids with their ambient environment.

The results, applicable to any other type of microresonator, provide insight into the relative importance of surface scattering and absorption centers in these cavities as well as the role of surface contaminants in altering the quality factor and thermal nonlinearities of these structures.

3-2 Thermal Bistability Effect

Thermal broadening/compression of the resonance line shape is frequently encountered in ultra-high-Q (UHQ) microcavities ($Q > 10^8$) [5]. As the laser frequency is swept across the cavity resonance, optical power coupled into the resonator is partially absorbed and converted to heat, hence altering the optical properties of the bulk medium and shifting the resonant frequency either along or opposite to the direction of laser scanning. In silica, the dominant effect is due to the temperature-dependent refractive index of the cavity material, which results in a negative frequency shift of the resonance with increased temperature:

$$(\nu - \nu_0) = -\nu_0 \frac{dn}{dT} \Delta T \quad (3.1)$$

where $(\nu - \nu_0)$ is the resonant frequency shift due to temperature change of ΔT , ν_0 is the initial resonant frequency, and dn/dT is the thermo optic coefficient of the cavity bulk material (i.e., the rate of refractive index change as a function of temperature). As a result, the resonance line-shape is distorted from its original Lorentzian profile, becoming broader when scanned towards lower frequencies and narrower when scanned in the opposite direction.

The characteristic equation for the optical power transmission spectrum in the presence of nonlinearity is given by the following equation:

$$1 - T = \frac{C}{1 + 4 \left[x + \frac{P_{in}}{P_{th}} (1 - T) \right]^2} \quad (3.2)$$

where T is the transmission beyond the resonator-waveguide coupling region and C is the criticality factor that determines the degree to which the resonator is coupled to the

waveguide ($0 \leq C \leq 1$) [6,7]. C starts at zero when the resonator is far from the waveguide (no coupling), reaches unity at the critical coupling point ($T=0$), and then declines toward zero as the resonator-waveguide coupling increases further and transmission recovers in the overcoupled regime. x is the normalized frequency defined as the deviation from the initial resonant frequency in units of resonator linewidth, i.e., $x = (\nu - \nu_0)/(\Delta\nu)$. The characteristic power in this equation, referred to as threshold power (P_{th}), is the required input power to shift a resonance by its linewidth.

Figure 3.1 shows how the resonant line-shape is modified from its original Lorentzian profile (achievable at $P_{in} \ll P_{th}$). The transmission spectrum appears as the ABC curve when the input laser is tuned towards lower frequencies and as the CDEA curve when scanned in the opposite direction. The minimum transmission ($T = 1 - C$) occurs at $x = -CP_{in}/P_{th}$, which shows that monitoring the thermal broadening as a function of launched power provides a tool for accurate measurement of threshold power for thermal bistability.

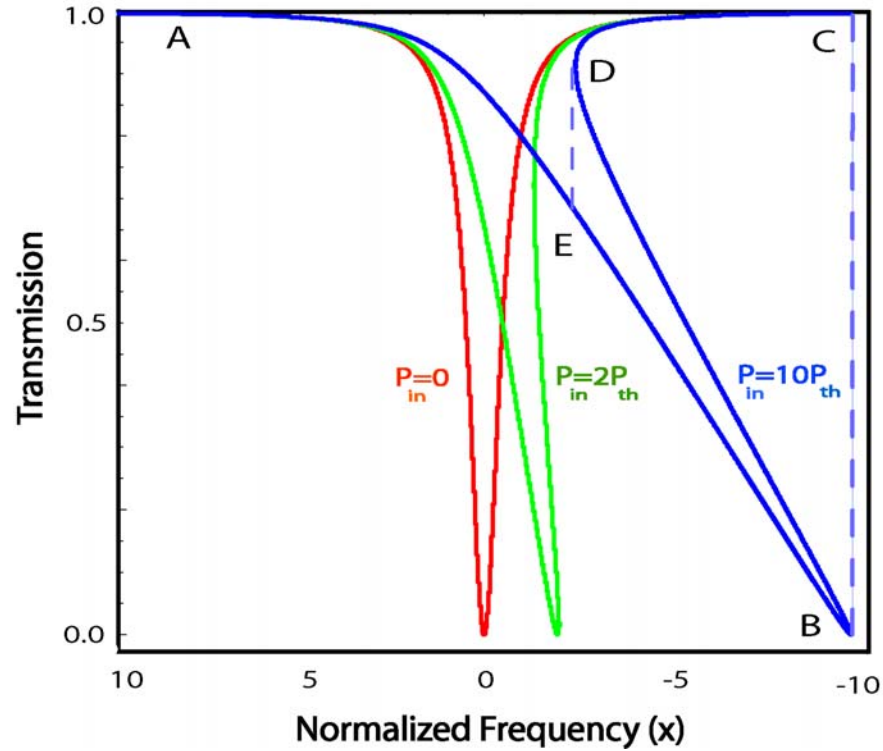


Figure 3.1: Thermal shift of the resonant frequency and distortion of resonant line-shape for different input powers. When $P_{in} \ll P_{th}$ the familiar Lorentzian profile is achieved; however for higher values of input power the typical thermal hysteric behavior can be observed. The ABC curve is the transmission spectrum of the resonator when the input laser is scanned towards lower frequencies and the CDEA curve shows its response in the reverse direction. The BD part of the curve is unstable.

For the thermal nonlinearity, threshold power is related to the resonator properties by the following form:

$$P_{th} \propto \frac{n v_0 C_p}{Q \alpha \tau_{thermal}} \frac{1}{dn/dT} \quad (3.3)$$

$C_p = \rho V_{eff} c_p$ is the heat capacity of the effective volume (V_{eff}) in the bulk medium where the heating occurs, ρ and c_p are the density and special heat capacity of the medium, respectively, and α is the absorption fraction of lost power (i.e., power lost to absorption relative to total power lost through all mechanisms contributing to intrinsic Q). From equation (3.3) P_{th} is inversely proportional to the quality factor (Q) and the thermal response time ($\tau_{thermal}$), which determines how fast the temperature of the optical mode volume rises.

3-3 Experimental Results

In order to excite the whispering gallery modes of microtoroids, fiber tapers were used to couple light into and out of the resonators [8]. Single-mode, tunable external-cavity lasers emitting in the 1550 nm, 1300 nm, and 980 nm bands were used as light sources. Transmission power through the fiber taper was monitored using fast photodiode detectors as the laser frequency was slowly (<10Hz) scanned over 10 GHz using a function generator.

Figure 3.2 shows the measured thermal shift of the resonant frequency vs. input power for a high Q ($Q \approx 0.9 \times 10^8$) whispering gallery mode of a toroid microresonator at two different wavelengths. Although Q values at these wavelengths are about the same, the threshold power at 970 nm is a factor of 20 higher than that at 1545 nm.

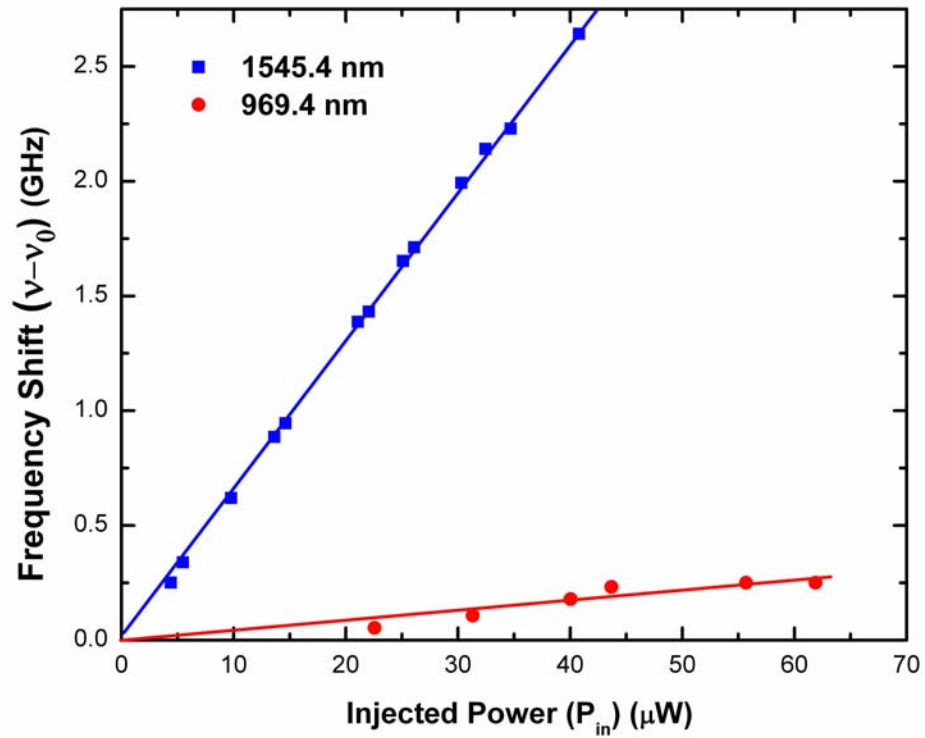


Figure 3.2: Shows thermal shift of the resonant frequency of a whispering gallery mode in a toroid microcavity as a function of coupled power to the resonator. The squares (blue) are the data at wavelength 1545.4 nm and the circles (red) are for the same fundamental transverse mode at 969.4 nm. The bistability threshold power is higher by a factor of 20 at 969.4 nm and is believed to be due to lower absorption of water at this wavelength.

From equation (3.3), the above difference suggests a higher absorption loss (higher α value) at 1545 nm compared to 970 nm. Such a difference in absorption cannot be explained in terms of silica absorption as fused silica is about 4 times more absorptive at 970 nm [9]. Absorption losses at 1550 nm, however, can be higher if there is a monolayer of water molecules on the resonator surface [10,11]. Figure 3.3 contains the calculated quality factor versus wavelength of a 60 μm diameter sphere (comparable to the microtoroids under study for the case of large toroidal minor diameters) that is limited by the combination of absorption due to a monolayer of surface water and the intrinsic absorption of fused silica. From this plot, a difference in threshold power of about 25 can be predicted using the calculated Q values alone (inversely related to absorption losses) at the measured wavelengths indicated in the Figure. The close agreement between the predicted and measured ratio of threshold powers at these wavelengths is thus consistent with the assumption of a water monolayer on the surface and suggests a highly efficient heat-transfer mechanism from the surface water layer to the bulk glass where the optical mode is mainly located.

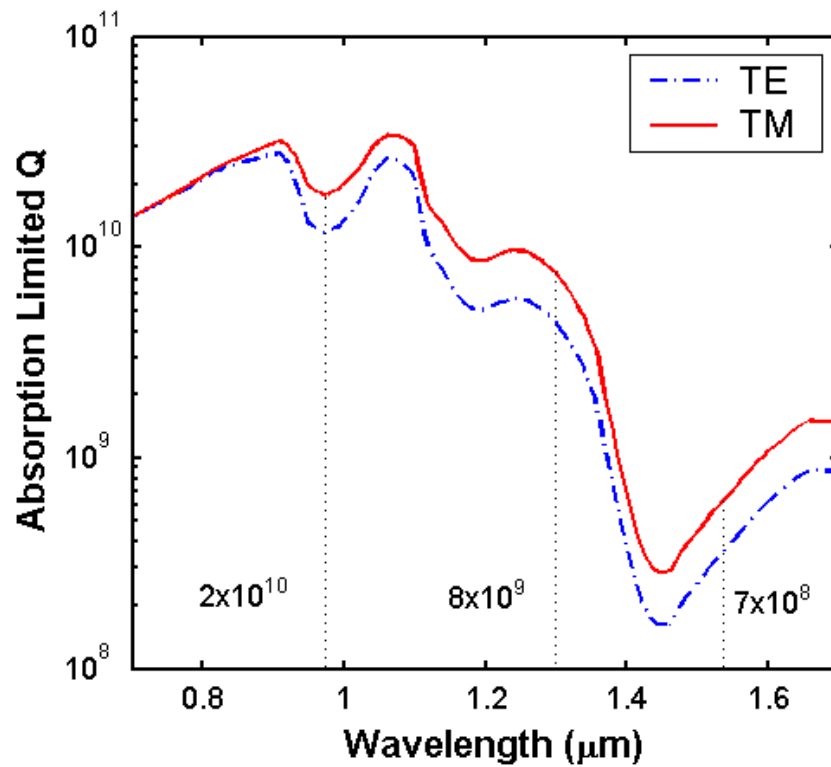


Figure 3.3: Calculated absorption limited quality factor of TE and TM fundamental WGM modes of a 60 μm diameter sphere. Absorption losses include the intrinsic bulk absorption of fused silica and that of a monolayer of water on the cavity surface. Predicted values for quality factor at 980 nm, 1300 nm, and 1550 nm wavelengths are marked in the figure.

From equation (3.3), threshold power is inversely proportional to the quality factor and the absorption fraction of lost power (α). In cases of exceptionally-smooth whispering-gallery surfaces (i.e., low scattering loss) and large diameter resonators (not whispering-gallery or bending-loss limited) the absorption fraction can approach unity (i.e., all the injected power converts to heat) and a Q^{-1} behavior of threshold power is expected. On the other hand, if non-thermal losses (scattering or bending losses) are the dominant loss mechanism, they determine the quality factor, and therefore the absorption fraction (here the ratio of thermal to non-thermal losses) would be proportional to Q . In such cases a Q^{-2} dependence in threshold power should be observable in modes belonging to the same resonator, but having different quality factors. In a regime where both losses are relatively important an intermediate behavior is expected.

Figure 3.4(a) shows the threshold powers measured for different modes of a scattering limited resonator. These WGM modes have Q 's ranging from 10^5 to 10^8 and they all lie within one free spectral range (9 nm) of the cavity. The data show a clear polynomial behavior with a slope of about -1.8 (close to inverse quadratic) in the 1550 nm band (circles). The data also show an exceptionally low threshold power (~ 10 nW) at 1550 nm. The same measurement on this resonator repeated in the 980 nm and 1300 nm bands reveals a similar behavior indicating that the quality factors in these cases are dominated by either surface roughness or scattering centers in the bulk material. The deviation from inverse quadratic behavior in these data can be due to the fact that distinct optical modes of the microtoroid have different extensions outside the cavity surface and hence experience differing water-absorption losses. This would in turn alter the

assumption of a Q^{-1} dependence of absorption fraction on quality factor in scattering limited resonators.

Figure 3.4(b) illustrates a resonator of similar size and quality factor but which exhibits absorption-limited behavior in the 1550 nm band (slope -1.1), scattering limited behavior in the 980 nm band (slope -1.9), and an intermediate behavior at 1300 nm (slope -1.6). By examination of Figure 3.2, this can be understood as resulting from variation in water absorption losses at these wavelengths.

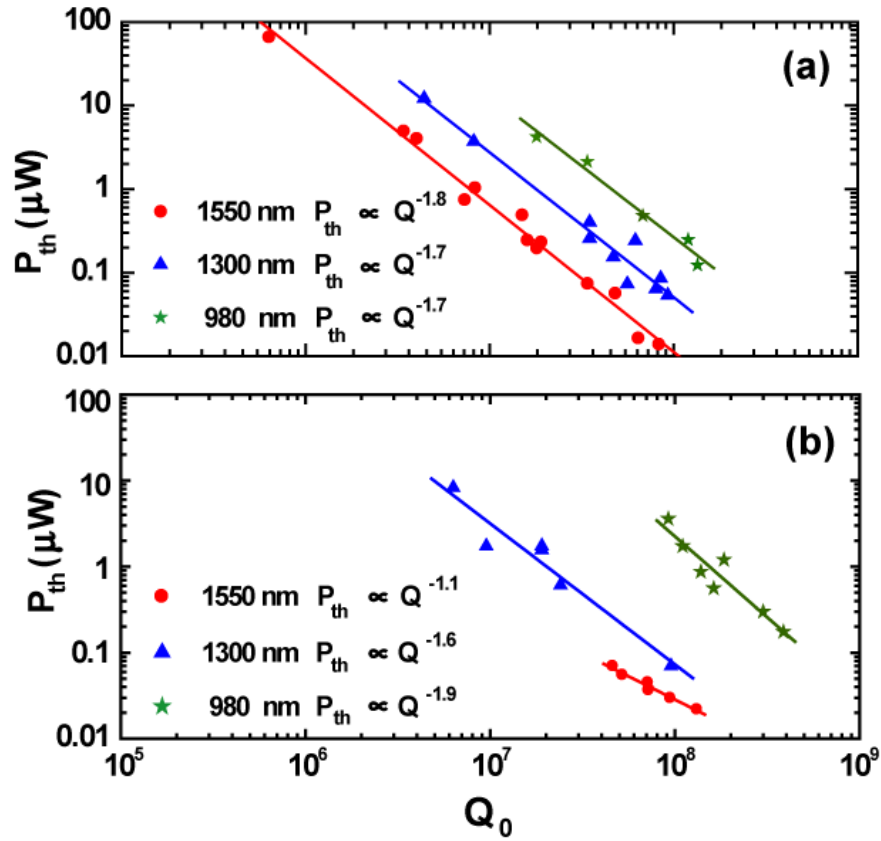


Figure 3.4: Thermal bistability threshold power as a function of quality factor for different WGM modes of a toroidal microresonator. (a) Shows a scattering limited case obtained in resonator 1. (b) Illustrates the data from a similar experiment on resonator 2. In this case, a monotonic increase in the slope of graphs from 1500 nm (circles) to 1300 nm (triangles) and 980 nm (stars) wavelengths shows the transition from absorption-limited to scattering-limited regime. Also the threshold powers increase as the input frequencies move to a more transparent part of the water absorption spectrum.

As further evidence that surface water layers play a major role in absorption losses of the microtoroids under consideration, we investigated the thermal bistability effect in humid environments. Figure 3.5 shows how the bistability threshold power at 1550 nm wavelength decreases as the environment becomes more humid. Significantly, the quality factor of the resonator in this measurement does not change noticeably as humidity is varied, which indicates that scattering is the dominant loss mechanism in this microtoroid. The change in threshold power therefore arises entirely from the change in absorption fraction parameter that can be directly related to the number of water molecules on the surface of the cavity.

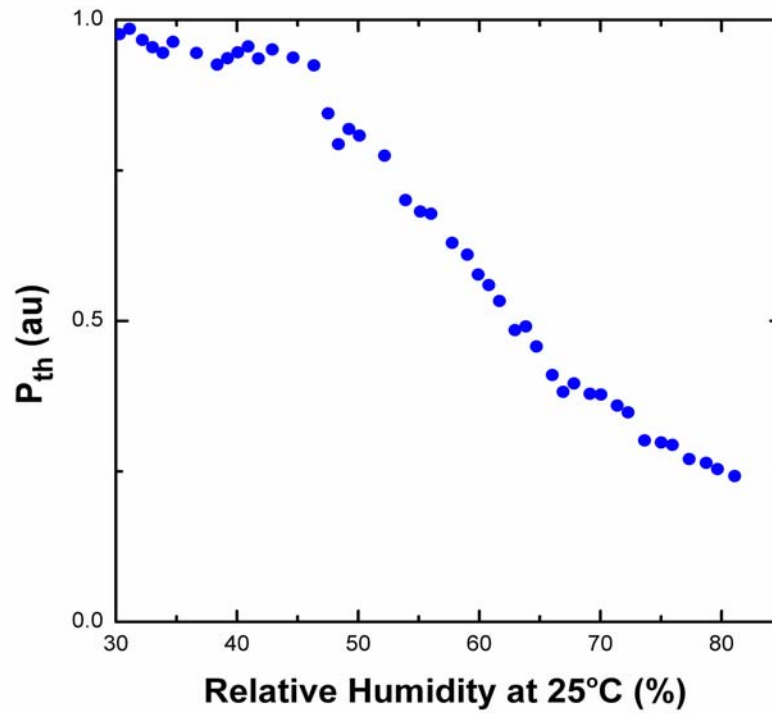


Figure 3.5: Thermal bistability threshold power as a function of humidity for a scattering-limited microtoroid. Although the quality factor of the resonator remains the same, the threshold power at 80% humidity drops to about a quarter of its value at humidity levels below 45%. The water molecules increase the absorption coefficient (α) as they adsorb onto the cavity surface, demonstrating the role of the surface water layers as the main source of absorption loss in the 1550 nm wavelength band.

3-4 Conclusions

Our findings in this chapter demonstrate that measurement of nonlinear thermal effects in microresonators is an effective method to characterize different loss mechanisms in these structures. In particular, the degree to which resonators are absorption limited or scattering limited can be inferred from measurement of threshold power versus Q . In cases where there is a strong spectral dependence of absorption centers (such as the case of water adsorbed onto silica), it is also possible to make this determination through a combination of spectral measurements of threshold power and Q . In the measurements presented, information was obtained about the surface chemistry of the cavity, which revealed the presence of mono-layers of water on the surface. Generalization of this method to other surface contaminants that could advertently be deposited on the surface of these structures can be potentially useful in sensing applications and surface chemistry studies. Furthermore, real time monitoring of thermal properties and quality factor can be beneficial in studying the dynamics of interaction between the resonator surface and its environment.

3-5 Bibliography

- [1] F. Treussart *et al.* Evidence for intrinsic Kerr bistability of high-Q microsphere resonators in superfluid helium. *European Physical Journal D*, 1(3): 235-238, 1998.
- [2] V. B. Braginsky, M. L. Gorodetsky and V.S. Ilchenko. Quality-factor and nonlinear properties of optical whispering-gallery modes. *Physics Letters A*, 137(7-8): 393-397, 1989.
- [3] V. S. Ilchenko, and M. L. Gorodetsky. Thermal nonlinear effects in optical whispering gallery microresonators. *Laser Physics*, 2: 1004-1009, 1992.
- [4] D. K. Armani, T. J. Kippenberg, S. M. Spillane, and K. J. Vahala. Ultra-high-Q toroid microcavity on a chip. *Nature*, 421(6926): 925-928, 2003.
- [5] L. Collot, V. Lefevre-Seguin, M. Brune, J. M. Raimond and S. Harche. Very high-Q whispering-gallery mode resonances observed on fused-silica microspheres. *Europhysics Letters*, 23(5): 327-334, 1993.
- [6] A. Yariv. Critical coupling and its control in optical waveguide-ring resonator systems. *IEEE Photonics Technology Letters*, 14(4): 483-485, 2002.
- [7] M. Cai, O. Painter and K. J. Vahala. Observation of critical coupling in a fiber taper to silica-microsphere whispering gallery mode system. *Physical Review Letters*, 85(1): 74-77, 2000.
- [8] S. M. Spillane, T. J. Kippenberg, O. J. Painter, and K. J. Vahala. Ideality in a fiber-taper-coupled microresonator system for application to cavity quantum electrodynamics. *Physical Review Letters*, 91(4): art. no. 043902, 2003.

- [9] D. A. Pinnow, T. C. Rich, F. W. Ostermayer, and M. DiDomenico. Fundamental optical attenuation limits in liquid and glassy state with applications to fiber optical waveguide materials. *Applied Physics Letters*, 22(10): 527-529, 1973.
- [10] M. L. Gorodetsky, A. A. Savchenkov, and V. S. Ilchenko. Ultimate Q of optical microsphere resonators. *Optics Letters*, 21(7): 453-455, 1996.
- [11] D. W. Vernooy, A. Furusawa, N. P. Georgiades, V. S. Ilchenko, and H. J. Kimble. Cavity QED with high-Q whispering gallery modes. *Physical Review A*, 57(4): R2293-R2296, 1998.

Chapter Four

Observation of Kerr Nonlinearity in Microcavities at Room Temperature

4-1 Introduction

Ultra-high quality factor (high Q) optical microcavities (e.g., microspheres and microtoroids) are ideally suited for observing nonlinear optical effects with extremely low (sub-microwatt) threshold powers [1-5]. The combination of high circulating power, made possible by high quality and strong confinement of this power within mode volumes of the order of hundreds of μm^3 , leads to inter-cavity circulating intensities in excess of $1 \text{ GW}/\text{cm}^2$ with only 1 mW of input power (assuming Q values of approximately 100 million in microtoroid resonators having principal diameters of about 50 microns.) This level of intensity is sufficient to unveil nonlinear phenomena even in materials like silica that are weakly nonlinear. The optical Kerr effect arises from the third-order susceptibility of the optical material, which results in intensity-dependent refractive index. This effect and a variety of its applications have been the subject of numerous research activities around the world [6]. The observation of this phenomenon in microcavities however is problematic as it is accompanied by relatively larger thermal nonlinear effects [4,5,7]. As studied in chapter 3, the refractive index of silica, which is also a function of temperature, varies as the circulating power is partially absorbed in the medium and the cavity temperature subsequently increases. This larger effect (thermo-optic effect) masks the Kerr-driven variations in the refractive index. F. Treussart et al. in

reference 5 have found evidence for Kerr bistability in microresonators by immersing microspheres in a superfluid helium bath at 2K. This cryogenic setup greatly reduces the sensitivity of WGM resonances to temperature and allows the Kerr effect to be dominant and hence observable. In terms of parameters introduced in chapter 3, the cryogenic setup reduces the thermal response time ($\tau_{thermal}$) by rapid extraction of heat from the resonator structure. This consequently increases the thermal bistability threshold power (see equation 3.3) suppressing the thermal nonlinearities.

In this chapter we propose and experimentally verify a method for observing the optical Kerr effect in microcavities at room temperature. The technique discriminates against the much larger and typically dominant thermal component of nonlinearity by using its relatively slow frequency response compared to the almost instantaneous Kerr effect. Measurement of the Kerr coefficient (n_2), or equivalently third-order nonlinear susceptibility of the cavity material ($\chi^{(3)}$), is demonstrated for the case of a silica microcavity. With this approach useful information about the characteristic thermal response time in microresonators can also be acquired.

4-2 Kerr-Nonlinearity Measurement-Approach

In order to manipulate the time response distinction in favor of Kerr effect, we use two beams (pump and probe) individually resonant with two WGM resonances of an optical microcavity. Modulation of the pump power results in the modulation of the cavity refractive index and consequently modulation of the resonant frequency of the WGM with which the probe beam is in resonance. The probe beam power transmission beyond the resonator waveguide junction therefore acquires a strong Fourier component at the modulation frequency of the pump beam. This component can be measured using a lock-in amplifier. When the pump modulation frequency becomes sufficiently faster than the thermal effects, the signal detected by the lock-in amplifier is purely due to the Kerr effect.

The modulated probe power (frequency Ω) is given by the following equation:

$$\frac{\Delta P_{probe}^{\Omega}}{P_{probe}} = P_{pump}^{\Omega} Q_{probe}^{total} Q_{pump}^{eff} \frac{2n_2 \lambda_{pump}}{\pi n^2 V_{eff}} C(x) \quad (4.1)$$

P_{probe} is the probe power coupled into the resonator and P_{pump}^{Ω} is the fraction of the pump power coupled into the cavity and carrying the modulation frequency Ω . The modulated probe power ($\Delta P_{probe}^{\Omega}$) depends on the refractive index change in the cavity as a result of the modulated pump power (P_{pump}^{Ω}), which is proportional to the quality factor of the cavity at pump wavelength (Q_{pump}^{eff}), n_2 coefficient, and the cross section of the optical mode. The changes in refractive index of the cavity cause variation of the probe power transmission, which greatly depends on the quality factor of the WGM coupled to the probe signal. Total quality factor of the optical mode at the probe frequency (ν_{probe}) is

given by Q_{probe}^{total} , which includes both intrinsic losses of the cavity and loading by the optical waveguide and can be obtained from linewidth measurements in the desired coupling regime. The transfer of modulation from pump to probe beam also depends on detuning of the cavity resonant frequency from that of the probe beam, which measured in units of linewidth of the cavity is denoted by x . The dependence $C(x) = 2x / (1 + x^2)$ is a number between one and zero depending on x (the deviation of the resonant frequency of the optical mode from the probe frequency in units of its linewidth). Q_{pump}^{eff} is the effective quality factor (defined below) of the resonator at the pump wavelength (λ_{pump}) and determines the enhancement of the pump power in the cavity [8]:

$$\frac{P_{pump}^{cavity}}{P_{pump}} = \frac{\lambda_{pump} Q_{pump}^{eff}}{\pi^2 n R} \quad (4.2)$$

where R and n denote the radius and refractive index of the cavity, respectively. Equation (4.3) below shows how Q_{pump}^{eff} can be obtained from the coupling parameter K defined as $K = Q_0 / Q_{ext}$, where Q_0 is the intrinsic quality factor of the optical mode and Q_{ext} is the quality factor associated with coupling to the optical waveguide.

$$Q_{pump}^{eff} = Q_0 \frac{K}{(1 + K)^2} \quad (4.3)$$

Finally, note in equation (4.1) that for a certain change in the refractive index of the cavity, higher Q modes experience larger transmission variations and hence the dependence of $\Delta P_{probe}^{\Omega}$ on Q_{probe}^{total} . Also observe the role of small mode volumes (V_{eff}) in reducing the required optical power for observation of nonlinear effects.

4-3 Experimental Results

The experimental set up used to observe and measure the Kerr nonlinearity of silica microcavities is shown in Figure 4.1. Two tunable external cavity diode lasers were used to generate the pump and probe beams in the 1550 nm and 1480 nm bands, respectively. The pump and probe laser frequencies are simultaneously tuned to two optical WGM resonances of a toroidal microcavity [9] and launched into a tapered optical fiber using a WDM coupler. Tapered optical fibers with waist diameters of 1-3 μm were fabricated by the traditional technique of simultaneous flame heating and pulling standard single mode (SMF-28) fibers [10]. Efficient and high ideality coupling to the optical modes of microtoroid cavities is possible using these waveguides [11]. A top view optical micrograph of a microtoroid evanescently side coupled to a tapered optical fiber is shown in Figure 4.1. The output of the 1550 nm laser is modulated using a Mach-Zehnder modulator (bandwidth 20 GHz) driven by an RF function generator that generates sinusoidal waves with frequencies up to 80 MHz. The detected signal due to residual transmitted modulated pump power in the probe channel could potentially mask the relatively small modulation in the probe power, and therefore two cascaded wavelength-selective couplers are used to ensure high extinction (above 38 dB) of the pump power in the probe channel. The pump and probe laser frequencies are adjusted while the detected pump and probe transmissions are monitored by an oscilloscope to ensure that both frequencies are tuned to the resonant frequencies of the cavity. A high precision PZT stage (10 nm steps) was used to position the microtoroid relative to the tapered fiber and thereby control the coupling to the resonator. With the laser frequencies tuned to proximity of the desired WGM resonances and with the pump power modulated, the

probe power is detected, and the photocurrent is processed by the lock-in amplifier using the output of the function generator as its reference signal. The lock-in was operated in the (r, θ) setting where r (in Volts) and θ (in degrees) are the amplitude and the relative phase of the detected signal at the reference frequency (Ω).

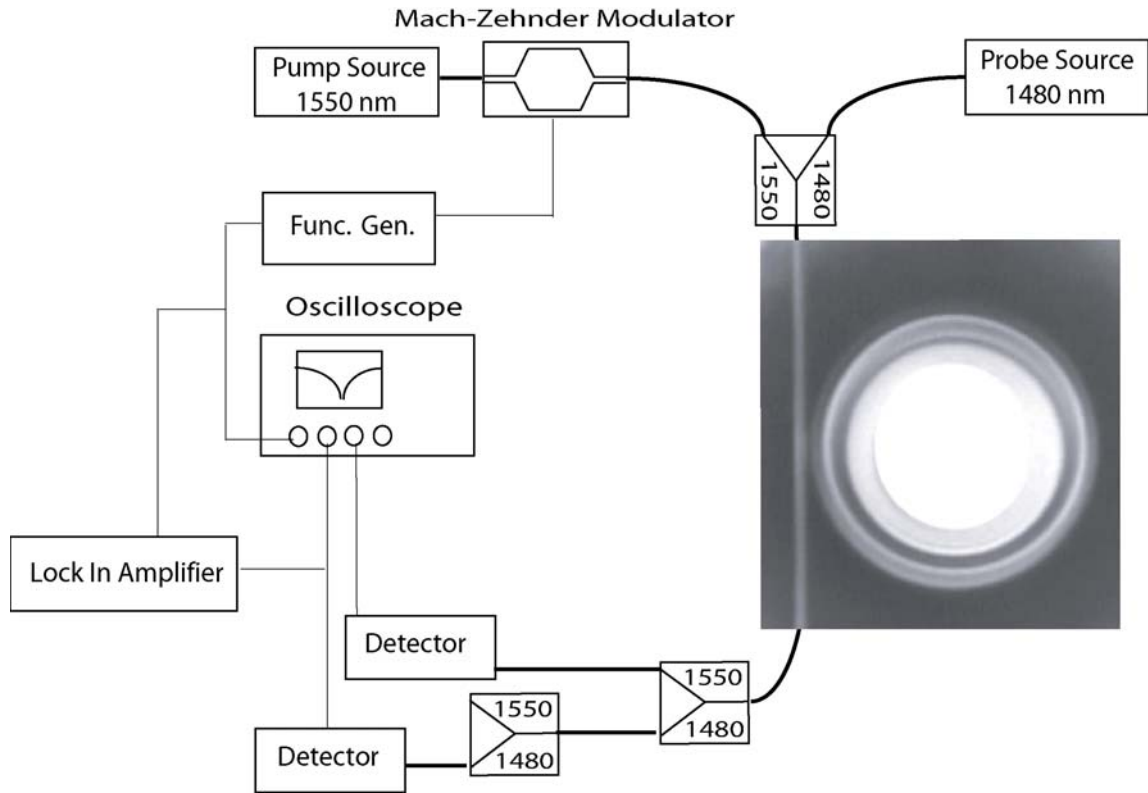


Figure 4.1: The experimental setup used for characterizing the Kerr nonlinearity of microcavities. The picture is a top-view optical micrograph of a toroid microresonator evanescently side coupled to a tapered optical fiber.

The output of the lock-in amplifier (r) in μV is plotted vs. the modulation frequency in Figure 4.2. This plot is normalized to the frequency response of the entire system with the microtoroid decoupled from the fiber taper. Therefore the plot shown in Figure 4.2 is the pure response resulting from the cross modulation of the probe beam by the pump beam. The power levels coupled to the resonator to generate the graph in Figure 2 were about $15 \mu W$ and $10 \mu W$ for pump and probe beams, respectively. Thermal effects can follow the modulation of the pump power up to about $\Omega = 10 KHz$, and hence a flat response is observed prior to this frequency. At higher frequencies however a decline in the amplitude response is observed with a 3 dB corner frequency of about 25 KHz suggesting a thermal response time in the order of $6 \mu s$. As mentioned in reference 4, the fastest thermal response time is associated with the conduction of heat generated in the optical mode volume to the cavity bulk material and can be put in the following compact form:

$$\tau_{thermal} = \frac{(\delta R)^2}{D} = \frac{1}{D} \left(\frac{2R\lambda^2}{\pi^2 n^2} \right)^{2/3} \quad (4.4)$$

where δR is the effective thickness of the optical mode localized near the surface of the cavity and D is the temperature conductivity of glass ($8 \times 10^{-3} cm^2 / s$). For the microtoroid under study here with major radius of $36 \mu m$ and minor diameter or thickness of about $8 \mu m$, the toroid geometry becomes similar to a sphere with respect to thermal effects within the modal volume. Applying the above expression to this sample predicts a thermal time constant of $5 \mu s$, which is in close agreement with the value derived from Figure 4.2.

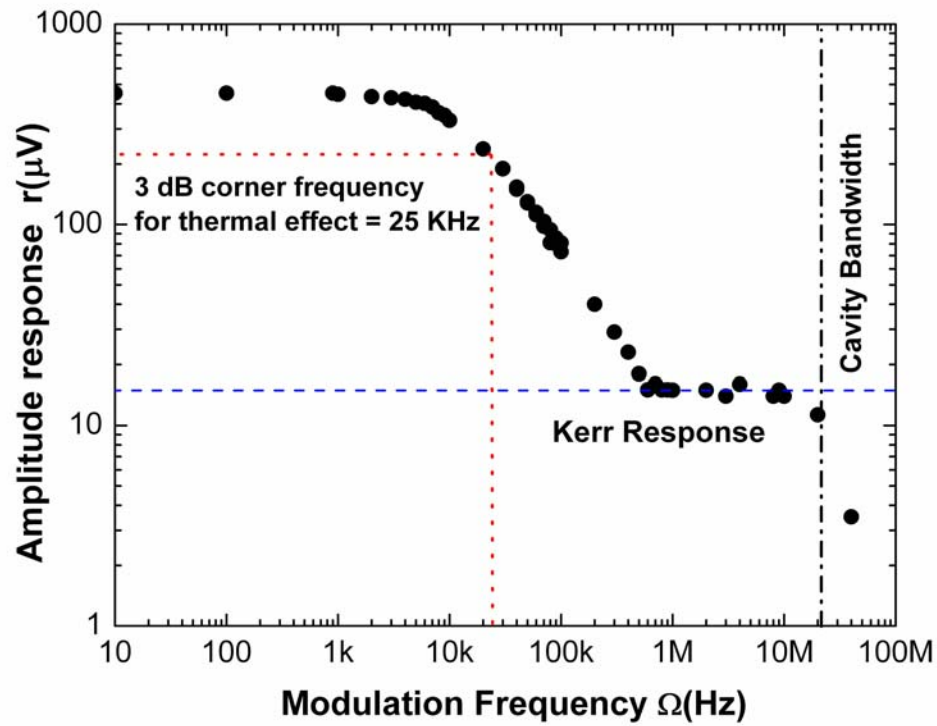


Figure 4.2: Measured amplitude modulation of the probe beam as a function of the modulation frequency of the pump power. The dotted lines show a 3 dB corner frequency of about 25 KHz where the modulation of the pump power becomes comparable to or faster than the thermal response time of the resonator. The second roll-off is due to limited bandwidth of the cavity that does not allow the pump power in the resonator to build up instantaneously. The flat response in the middle shows the “fast” Kerr effect.

Returning to Figure 4.2, the decline in the amplitude response continues until it reaches a second plateau from around 600 KHz to 10 MHz, which is far beyond the modulation speeds that thermal effects can follow. To ensure that this flat response was not due to the noise level arising from residual pump power in the 1480 nm channel or from RF crosstalk, the probe power was switched off during data acquisition in the flat portion of the spectrum. This resulted in the lock-in response decreasing by a factor of 40, thereby confirming that the measured response is associated with modulation of the probe wave. Furthermore, by calibrating the lock-in amplifier, the modulated probe power could be inferred (i.e., $\Delta P_{probe}^{\Omega}$). Plugging this inferred power into equation 4.1, we obtain an n_2 value of $(6 \pm 4) \times 10^{-16} \text{ cm}^2 / \text{W}$, which agrees well with measured n_2 values for fused silica ($n_2 = 3 \times 10^{-16} \text{ cm}^2 / \text{W}$). We therefore attribute the flattened response region in Figure 4.2 to the Kerr nonlinearity.

Equation (4.1) shows that the signal level at frequency Ω can be preserved for lower Q optical modes at the cost of higher optical input powers. We confirmed this by repeating the same measurement for different quality factor WGM resonances both within the same cavity and other microtoroids. By doing this, the flat Kerr response has been observed and the inferred n_2 coefficient has been obtained in numerous test samples. The flat Kerr response in the plot ultimately falls off due to the limited bandwidth of the optical mode. The optical field in the cavity is built up in a finite period, which is roughly equal to the inverse of the optical mode linewidth. At modulation frequencies higher than the cavity linewidth, the modulation of the pump power cannot fully build up within the cavity and be transferred to the probe beam. The WGM excited in the sample studied in Figure 4.2 had a loaded Q of about 10^7 , which translates to a

linewidth of about 20 MHz at 1550 nm. Using lower Q optical modes on the other hand, we could extend the Kerr plateau to higher frequencies.

4-4 Conclusions

This chapter demonstrates a powerful approach to observe Kerr nonlinearity in microcavities with extremely low optical powers. The simple experimental setup and room temperature operation of these measurements are attractive for studying nonlinear phenomena in microcavity structures. The discussed method is capable of measuring the nonlinear susceptibility of the cavity material and can be used to characterize the n_2 coefficient for different materials packaged in a microcavity-type structure.

4-5 Bibliography

- [1] R. K. Chang and A. J. Campillo (eds). Optical Processes in Microcavities. *World Scientific, Singapore*, 1996.
- [2] S. M. Spillane, T. J. Kippenberg, and K. J. Vahala. Ultralow-threshold Raman laser using a spherical dielectric microcavity. *Nature*, 415(6872): 621-623, 2002.
- [3] V. S. Ilchenko, A. A. Savchenkov, A. B. Matsko, and L. Maleki. Nonlinear optics and crystalline whispering gallery mode cavities. *Physical Review Letters*, 92(4), art. no. 043903, 2004.
- [4] V. S. Ilchenko, and M. L. Gorodetsky. Thermal nonlinear effects in optical whispering gallery microresonators. *Laser Physics*, 2: 1004-1009, 1992.
- [5] F. Treussart *et al.* Evidence for intrinsic Kerr bistability of high-Q microsphere resonators in superfluid helium. *European Physical Journal D*, 1(3): 235-238, 1998.
- [6] Robert W. Boyd. Nonlinear Optics. *Academic Press, Boston, c*, 1992.
- [7] V. B. Braginsky, M. L. Gorodetsky, and V. S. Ilchenko. Quality-factor and nonlinear properties of optical whispering-gallery modes. *Physics Letters A*, 137(7-8): 393-397, 1989.
- [8] H. Haus. Waves and Fields in Optoelectronics. *Prentice-Hall, Englewood Cliffs, N.J.*, 1984.
- [9] D. K. Armani, T. J. Kippenberg, S. M. Spillane, and K. J. Vahala. Ultra-high-Q toroid microcavity on a chip. *Nature*, 421(6926): 925-928, 2003.
- [10] M. Cai, O. Painter and K. J. Vahala. Observation of critical coupling in a fiber taper to silica-microsphere whispering gallery mode system. *Physical Review Letters*, 85(1): 74-77, 2000.

- [11] S. M. Spillane, T. J. Kippenberg, O. J. Painter, and K. J. Vahala. Ideality in a fiber-taper-coupled microresonator system for application to cavity quantum electrodynamics. *Physical Review Letters*, 91(4): art. no. 043902, 2003.

Chapter Five

Radiation-Pressure-Induced Mechanical Oscillations (Parametric Instability) in Optical Microcavities

5-1 Introduction

Radiation pressure can couple the mechanical modes of an optical cavity structure to its optical modes, leading to parametric oscillation instability. This regime is characterized by regenerative oscillation of the mechanical cavity eigenmodes. In this chapter, we present the first observation of this effect with a detailed theoretical and experimental analysis of these oscillations in ultra-high-Q microtoroids. Embodied within a microscale, chip-based device, this mechanism can benefit both research into macroscale quantum mechanical phenomena and improve the understanding of the mechanism within the context of Laser interferometer gravitational-wave observatory (LIGO). It also suggests that new technologies are possible that will leverage the phenomenon within photonics.

5-2 Parametric Instability

As circulating power is boosted in optical resonant systems there will be a natural tendency for these systems to experience a radiation-pressure induced instability. The instability is manifested as regenerative oscillations of the mechanical modes of the cavity structure due to coupling of optical and mechanical degrees-of-freedom caused by radiation pressure. This has been recognized theoretically by V. Braginsky [1,2] and is termed “parametric oscillation instability.” At a simplistic level, this excitation process can be understood as follows. Each circulating photon in the cavity changes its propagation direction twice every roundtrip. Therefore, a photon transfers 4 times its linear momentum to the cavity walls every time it completes a round trip. If the cavity is not infinitely rigid, the walls will deform in response to the resulting pressure. Hence, the pressure of circulating radiation induces a mechanical expansion of the cavity structure. This motion, in return, takes the optical cavity out of resonance with the input pump wave, thereby lowering the magnitude of radiation force. Upon restoration of the mechanical deformation, the process resumes, leading to a periodic motion of the cavity as well as the circulating power. It should be emphasized that this oscillation is regenerative, exhibiting classic threshold behavior and requiring no external modulation of the pump wave (see Figure 5.1)

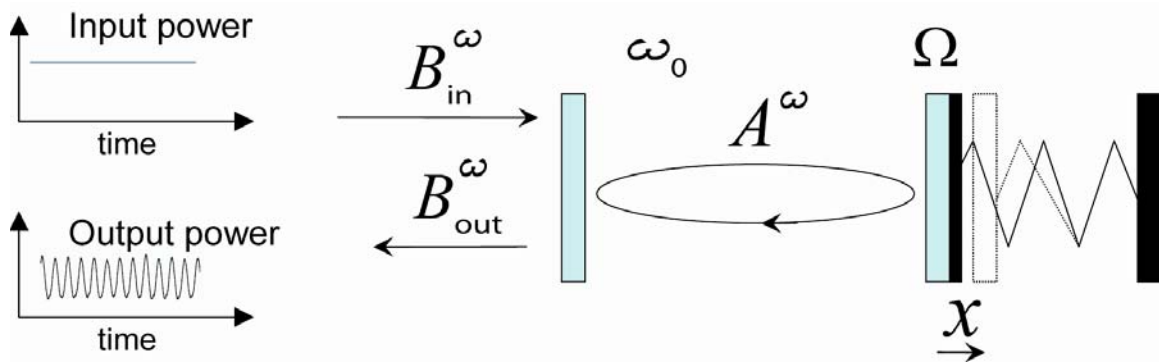


Figure 5.1: Illustration of the radiation-pressure induced optomechanical coupling mechanism. B_{in}^ω , the input optical field (at frequency ω close to a resonant frequency of the cavity ω_0) to the Fabry-Perot, causes large circulating field A^ω as a result of resonant power-buildup in the cavity. The pressure caused by this power moves the free-to-move cavity wall by x , modeled as a damped harmonic oscillator at frequency Ω . Motion of the end mirror on the other hand causes frequency change of the Fabry-Perot resonant optical mode. This interaction at sufficient optical powers results in regenerative oscillations of the end mirror and consequently the modulation of the output optical power B_{out}^ω .

More precisely, if one assumes the optical pump-wave frequency (ω) is nearly resonant (but not exactly resonant) with the optical mode, radiation-pressure induced deformation of the cavity structure either lowers or raises the coupled optical pump power, depending upon the sign of detuning of the pump frequency relative to the cavity resonant frequency. It will be shown that when the pump laser is detuned to the high-frequency tail of the optical mode, the phase relationship between optical pressure and optical cavity deformation results in net power transfer from the optical pump to the mechanical mode. This transfer manifests itself mathematically as a gain for the mechanical oscillations, with a corresponding threshold optical pump-power.

Numerous theoretical studies have been devoted to ramifications of this effect in the context of the Laser Interferometer Gravitational-Wave Observatory (LIGO) [3.4]. It was predicted during the past few years [1-6] that the parametric instability could limit the maximum stored energy in Fabry-Perot cavities (FP) used in the LIGO project and hence the sensitivity of the gravitational wave detector. Although never observed, recently a bench top experimental setup was proposed to verify these theoretical concerns on a smaller scale [7].

As will be discussed in detail in the next sections, the mutual coupling of optical and mechanical modes is significantly enhanced in smaller size cavities. Whereas in macroscopic resonators the influence of radiation pressure is weak and only appreciable at high power levels [8], it is significant in optical microcavities (such as silica microspheres [9], microdisks, or microtoroids [10]), which simultaneously exhibit ultra-high-Q optical modes *and* small mechanical mass. As discussed in previous chapters, when coupled to a waveguide, the high quality factor of whispering-gallery microcavities

($\sim 10^8$) results in optical power build-up that can exceed 100 Watts of circulating power for only 1 mWatt of waveguide input power. The resulting radiation pressure due to confinement of these high optical powers in micron-scale volumes can expand the cavity structure such that the optical resonant frequency shifts by hundreds of the resonance linewidths. Therefore the combination of high optical quality factor and small mechanical mass and dissipation can lead to threshold levels in the microwatt regime for regenerative mechanical oscillations (i.e., parametric oscillation instability) in whispering-gallery microcavities.

Radiation-pressure-induced optomechanical interaction has similar properties to cavities containing a Kerr medium [11] (see chapter 4), including hysteretic wavelength response caused by radiation pressure [8]. In particular, both radiation pressure and the Kerr effect induce a coupling between optical path length and light intensity, one through cavity strain and the other through the index of refraction. It is therefore not surprising that radiation pressure has been proposed as an alternative path for observation of quantum effects such as squeezing [11]. Radiation pressure acting on a movable cavity can transfer information between two systems initially in semiclassical states, which, in turn, become entangled. Using this entanglement it is possible to perform Einstein-Podolsky-Rosen (EPR) tests [12]. Also, the possibility of teleporting and storing the quantum information carried by the radiation field in the vibrational state of a macroscopic cavity through ponderomotive entanglement is proposed recently [13,14]. Moreover, the nature of radiation pressure to act on a macroscopic object suggests that it is a promising mechanism for entangling macroscopic mechanical oscillators [13], creating a Schrödinger cat state of a macroscopic mirror [15] and teleportation of a

macroscopic mechanical resonator state [16]. Standard quantum-limited measurements of position [17] are other exciting areas where this interaction can become useful.

5-3 Transmission Oscillations and Mechanical Eigenmodes of Microtoroids

In this chapter we will focus on the radiation-pressure-induced parametric instability in whispering-gallery microtoroid resonators [10]. However, all the aspects of this work may apply in principle to any type of optical cavities.

This section reports the observation of transmission oscillations in the radio-frequency (RF) range when optical power is coupled to sufficiently high quality factor optical modes ($Q \approx 10^7$ or 10 ns photon lifetime at infra-red wavelengths) of toroidal microcavities [18,19,20] (see Figure 5.2.)

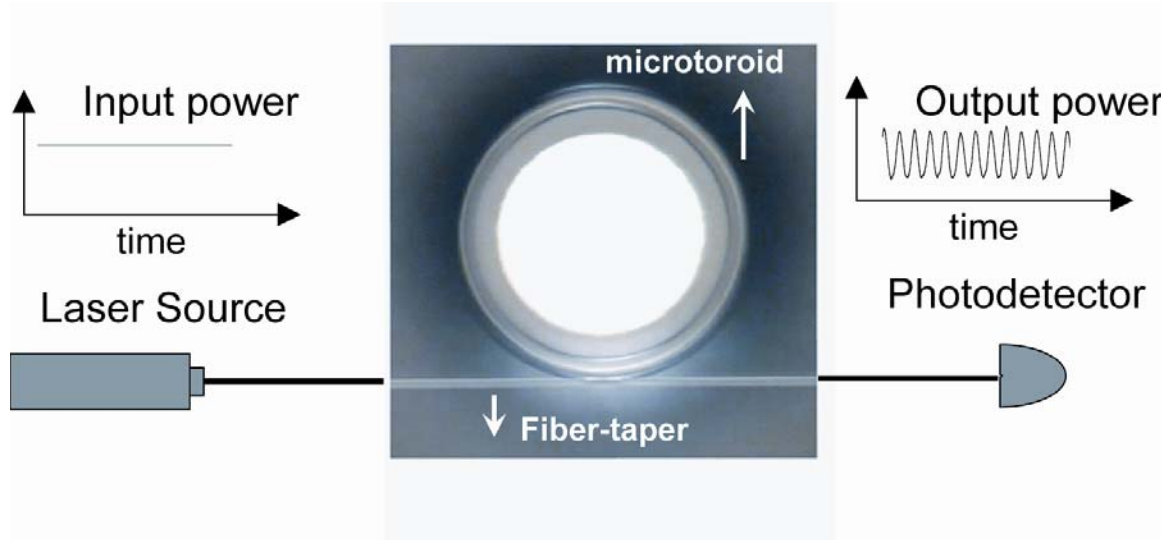


Figure 5.2: The schematics of the simple experimental setup used for observation of transmission oscillations in toroid microcavities. The DC optical power of a laser source is coupled to a microtoroid through a tapered optical fiber. The transmitted optical power shows high amplitude modulations in the radio frequency range upon detection by a photodetector.

Spectral analysis of the detected transmitted optical power using a high-resolution electrical spectrum analyzer (ESA) revealed extremely narrow peaks (sub-Hertz linewidths) at a frequency typically in the range of 10-100 MHz as well as at harmonics of this fundamental frequency (see Figure 5.3). As can be seen in Figure 5.3, typically two distinct fundamental oscillation frequencies (and their harmonics [21]) were observed: a low frequency mode (~ 2 -20 MHz) usually in the under-coupled regime and a high frequency mode (~ 40 -100 MHz) in the over-coupled regime (see reference [22] and references therein for definition of under-, critical-, and over-coupled regimes).

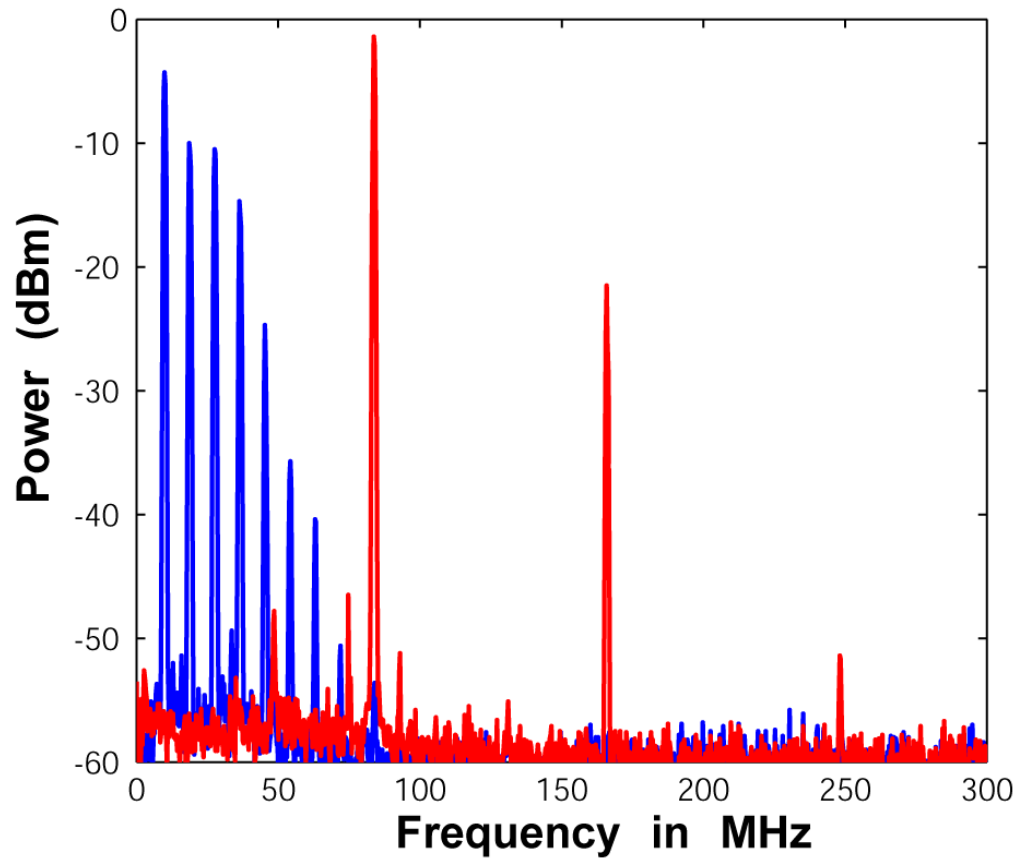


Figure 5.3: The measured, spectral content of pump-power (at 1550 nm) transmission as observed on an electrical spectrum analyzer (bandwidth set at 100kHz). Two families of frequencies are observed along with their harmonics. Those at lower frequency range are observed generally in the undercoupled regime and the higher frequency oscillations mostly in the overcoupled regime.

Our further studies of this phenomenon revealed that in addition to their excellent optical properties, microtoroid resonators also exhibit high-Q micromechanical modes, which are flexural or radial in character and exhibit experimentally observed Q-factors as high as 5000. We numerically investigated the mechanical eigenmodes of a toroidal structure. The right panel of Figure 5.4 shows the strain and stress of the first three rotationally symmetric eigenmodes of a toroid microcavity obtained by finite-element modeling. The left panel of Figure 5.4 shows the experimentally observed oscillation frequencies plotted versus length L (see right panel for definition of L) as inferred by scanning electron microscopy (SEM) imaging. As is evident, the frequencies increase with decreasing membrane length (L). Close agreement of the measured RF oscillation frequencies with the results of the numerical modeling (less than 5% discrepancy) confirms that the first- ($n=1$) and third- ($n=3$) order flexural modes are responsible for generating the observed low- and high-frequency families of oscillations, respectively (see Figure 5.3). It will be explained later in the chapter why $n=2$ mode is extremely hard to observe in our experiments.

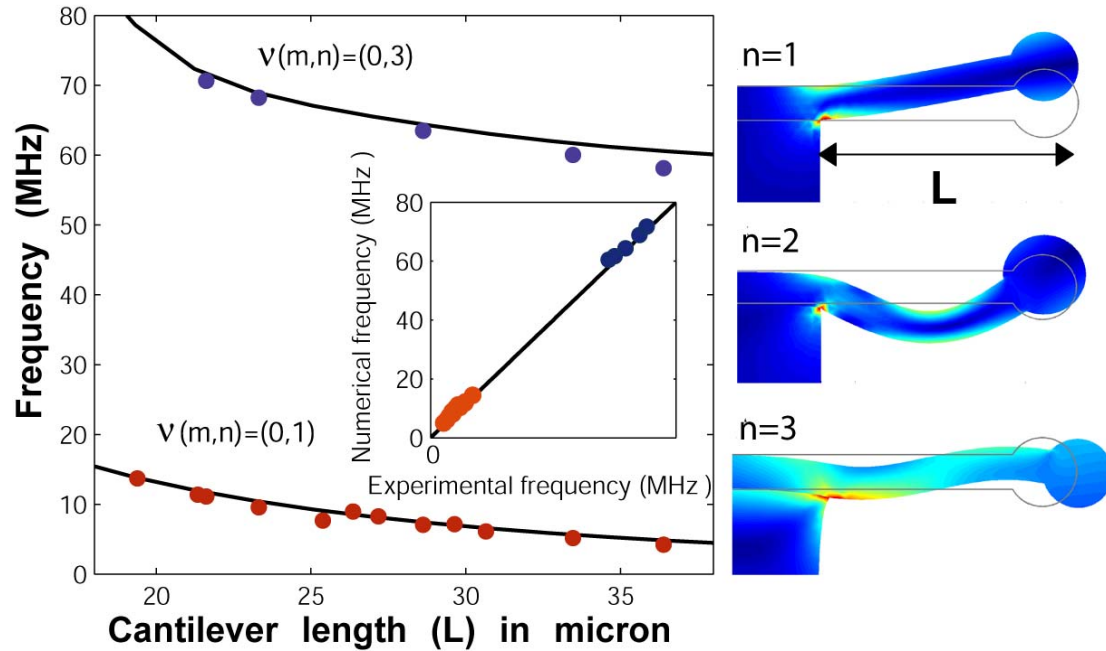


Figure 5.4: Right Panel: Finite element modeling of the micromechanical modes of a silica toroid microcavity. The radial and azimuthal mode order are denoted with n and m (where $m = 0$ corresponds to rotationally symmetric modes). Shown are the first three rotationally symmetric radial modes ($n = 1, 2, 3, m = 0$) in cross section with the amplitude of motion greatly exaggerated for clarity. In addition, the stress field is indicated using color. Note that the mechanical motion modulates the cavity path length due to a change in the cavity radius. Left Panel: Mechanical oscillation frequencies of the ($m=0,n=1$) and ($m=0,n=3$) modes versus the cantilever length L (defined in the right panel). Dots are experimentally measured frequencies and the solid lines are predictions of the numerical modeling. Inset shows the agreement between the numerical predictions of mechanical frequencies and measured frequencies of oscillations.

The mechanical origin of these oscillations was also confirmed by lowering a metallic microprobe into proximity with the plane of the silica disk connecting the toroid to the silicon pillar (i.e., not the toroid itself, where the optical mode lies). Since the probe is far removed from the toroidal whispering gallery, it affects only the mechanical and not the optical properties of the structure. The optical power oscillations were observed to fully quench upon probe contact.

As evident in Figure 5.4, the $n=3$ mechanical mode has a strong radial component to its motion and hence understanding of its excitation by way of radiation pressure (which itself is primarily radial in direction) is straightforward. In contrast, the $n=1$ mode motion is transverse, requiring a different method of force transduction (see Figure 5.5). The details will be presented in section 5.7 where it is shown that minute offsets of the optical mode from the equatorial plane provide a moment arm for action of radiation pressure. The resulting torque induces the transverse motion associated with the $n=1$ mode. Modelling and SEM measurement of the offset, via focused ion beam preparation, confirms this mechanism (also see Figure 5.13).

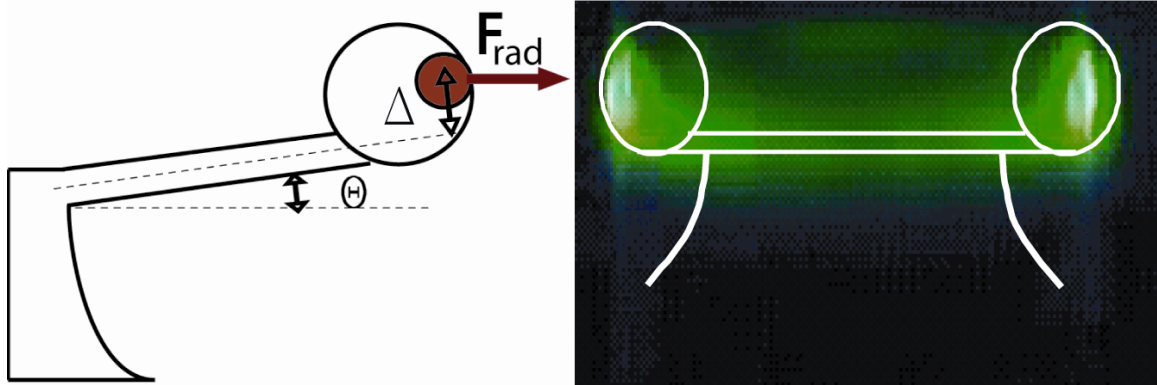


Figure 5.5: Left panel shows the cross section and excitation mechanism of the fundamental ($n=1$) flexural mode. The offset (Δ) between the optical mode location and the disk equatorial plane creates a lever arm for the radial optical force (F_{rad}) and, subsequently, a torque. Right panel shows the side-view image of a toroidal microcavity pumped by CW laser at 1550 nm. Green luminescence is the result of Erbium up-conversion (from 1.5 to 0.5 μm) which is intentionally doped in the microtoroid to illustrate the location of the optical mode. Note that the optical mode (green) is higher than the “cantilever beam” holding the microtoroid attesting the existence of the offset (Δ) in the left panel.

5-4 Equations of Motion for Optical and Mechanical Resonators and Adiabatic Approximation

The system described above can be modeled using a set of coupled differential equations: one, governing the harmonic motion of the flexing toroid and a second governing the resonant optical field. The equation of motion for deformation (more precisely, the displacement of the whispering gallery in the radial direction (x)) is that of a damped, harmonic oscillator driven by radiation pressure (generated by the circulating optical field at the periphery of the microtoroid):

$$\ddot{x}(t) + \gamma_0 \dot{x}(t) + \Omega^2 x(t) = \frac{f(t)}{m_{\text{eff}}} = \frac{2\pi n}{m_{\text{eff}} c} |A(t)|^2 \quad (5.1)$$

where m_{eff} is the effective vibrating mass of the mechanical structure in the radial direction (the direction that alters the optical resonant frequencies of the cavity), Ω is the mechanical frequency of the oscillation (one of the eigenfrequencies of the structure), and γ_0 is the intrinsic mechanical damping coefficient determining the mechanical quality factor $Q_m = \Omega/\gamma_0$. $f(t)$ is the radial force applied by radiation pressure of the slowly varying field amplitude, $A(t)$ (normalized so that $|A(t)|^2$ is the circulating optical power). c/n is the velocity of light in the cavity. As the optical resonance shifts with structure expansion, the frequency difference between the input field and the moving-cavity resonance changes as:

$$\Delta\omega(t) = \Delta\omega_0 - (\omega_0 / R)x(t) \quad (5.2)$$

Here R represents the radius of the microcavity (or more precisely, of the optical whispering-gallery mode). The mechanically induced displacement of the optical cavity

resonant frequency contains, in general, a contribution from spatial and refractive index changes (stress optical effect) [23,24]. The optical field in the cavity on the other hand obeys the following equation [25]:

$$\dot{A}(t) + A(t) \left[\frac{\omega}{2Q_{tot}} - i \Delta\omega(t) \right] = i B \sqrt{\frac{\omega}{TQ_{ext}}} \quad (5.3)$$

B is the input pump field (normalized such that $|B|^2$ is optical power launched in the waveguide.) Q_{total} is the total quality factor of the optical mode, made up of an intrinsic contribution Q_0 and a waveguide-loading contribution Q_{ext} : $1/Q_{total} = 1/Q_0 + 1/Q_{ext}$ (see ref. [22]). T is the photon round-trip time in the cavity.

In this section we will solve the above system of equations assuming what we will call the ‘‘adiabatic approximation.’’ This approximation holds when $\Omega \ll \omega/Q_{tot}$ (i.e., mechanical frequency is much smaller than the optical cavity bandwidth). The adiabatic picture provides a clear and intuitive understanding of the described optomechanical interaction. In section 5.6 we will solve the system with a more general approach, revealing the details of this interaction.

In the adiabatic regime, equations 5.1-5.3 can be solved self consistently, leading to a mechanical gain term that is a linear function of the circulating optical power and that offsets intrinsic sources of mechanical damping as given below. This leads to a threshold optical pump power for onset of mechanical oscillations as follows:

$$\gamma = \gamma_0 (1 - P/P_{threshold}), \quad P_{threshold} = \frac{R^2 \omega_0^2 m \Omega}{64} f(d) \frac{Q_{ext}}{Q_{total}^4 Q_m} \quad (5.4)$$

where the intrinsic mechanical damping coefficient γ_0 is modified to γ in presence of the optical power in the waveguide (P) and where $P_{threshold}$ denotes the incident threshold power (power in the waveguide, not the power coupled into the resonator).

At strong coupling regimes ($Q_{ext} \ll Q_0$) the overall quality factor is dominated by waveguide loading (i.e., $Q_{tot} \approx Q_{ext}$), and hence equation (5.4) predicts that in this regime, the threshold power scales approximately with $1/Q_{total}^3$ emphasizing the importance of high optical Q. Also apparent from equation 5.4 is the rapid scaling of the threshold power with cavity dimensions. Taking into account the scaling of the effective vibrating mass and its frequency, threshold power scales approximately with $P_{threshold} \propto R^4$. This explains why this effect, not yet observed in the context of the LIGO project, is more likely to occur in microcavities with high Q factors and small dimensions.

In equation 5.4, d is the detuning factor, giving the normalized detuning of the optical frequency from the resonant optical pump frequency of the cavity (ω_0) in units of its linewidth (i.e., $d \equiv \frac{\omega - \omega_0}{2\omega_0 / Q_{total}}$) and, $f(d) = (1 + d^2)^3 / d$ is a factor that is positive for blue-detuning of the pump (and negative for red detuning). This factor, emerging from the analysis, reflects the intuitive picture described earlier, requiring a particular phase relation between variation in coupled radiation pressure and cavity deformation in order that power is transferred from the optical mode to the mechanical mode and not in the opposite direction [26].

Analyzing the above system in time domain, by numerically solving the coupled differential equations 5.1-5.3, offers a clear picture of the energy flow between

mechanical and optical fields and the of interaction between the mechanical and optical resonators both present in the same device. Applying the predictor-corrector Adams' method on equations 5.1-5.3 reveals the system dynamical behavior $(A(t), x(t))$. Having $A(t)$ one can calculate the output power, $|(1 - T\omega/2Q_{tot})B + i\sqrt{T\omega/Q_{tot}}A(t)|^2$ [25]. Mechanical oscillations typically evolve to their full extent (starting from mechanical rest) within 5 time-constants of the mechanical structure $(10/\gamma)$. For small oscillation amplitudes $(x \ll R/Q_{tot})$ a nearly linear amplitude relation exists between mechanical motion and output power modulation. For larger oscillations, however, the system response becomes nonlinear as the microstructure vibrates faster than the optical power can build up in or discharge from the cavity (see Figure 5.6). Interference of the stationary pump wave and the field discharged from the cavity results in a train of decaying peaks reflecting the fact that light discharged from the cavity is decaying exponentially with time and is frequency shifted due to cavity vibrations. This behavior of output power is depicted in Figure 6a,b. At even larger oscillation amplitudes, we have also observed regimes where the system becomes sensitive to infinitesimal noise in the initial conditions when a specific threshold power is exceeded, resembling the chaotic behavior of the damped, driven pendulum.

Figure 5.6 shows the numerically solved cavity deformation, optical power in the cavity, and their interaction during a few mechanical time cycles. Cavity motion, $r(t)$ (not to be confused with radial part of it, $x(t)$), exhibits a flex of a few $\overset{\circ}{\text{Å}}$ corresponding to a resonance shift of few cavity bandwidths (Figure 5.6c). Cavity velocity $(\partial_t r(t))$ is about 0.9 mm/s when the cavity resonance crosses the pump laser wavelength (Figure 5.6d).

The cavity is then charged to a circulating power ($|A(t)|^2$) that approaches 50 W (Figure 5.6e) causing a centrifugal radiation force (f) that approaches $1.4 \mu N$. Upon cavity expansion, the power ($f(t)\partial_t \mu r(t)$) applied by radiation on the moving structure approaches 0.2 nW (Figure 5.6f). The resulting transference of energy is manifested as a red Doppler shift in the circulating photons. Upon the cavity shrinkage, power flows back to the optical mode from the mechanical potential energy; the circulating photons then experience a blue Doppler shift. A significant point is again the need for the pump wave to be blue detuned with respect to the microcavity resonance ($d > 0$ in equation 5.4) in order to induce oscillations. Because of this detuning, the pump wave spends a little more time to one side of the microcavity resonant frequency (Figure 5.6c) explaining why energy ($\int_0^t f(t')\partial_t \mu r(t')dt'$) flows on average from the optical mode to the mechanical mode (Figure 5.6g) and generates gain for mechanical vibrations as predicted by equation (5.4.) In this example, for each acoustical cycle, 9×10^{-18} Joules of energy are given to the optical mode upon shrinking, but then 10×10^{-18} Joules are taken from the optical mode upon expansion (Figure 5.6g). This energy difference drives the mechanical vibrations. The sign of the energy flow will be reversed if the pump detuning changes sign. It is interesting, and the reader can verify that the net energy transferred to the mechanical mode in every cycle (10^{-18} Joules) is equal to the dissipated mechanical energy (stored mechanical energy divided by the mechanical quality

factor, $E_{dissipated} = \frac{2\pi E_m}{Q_m}$).

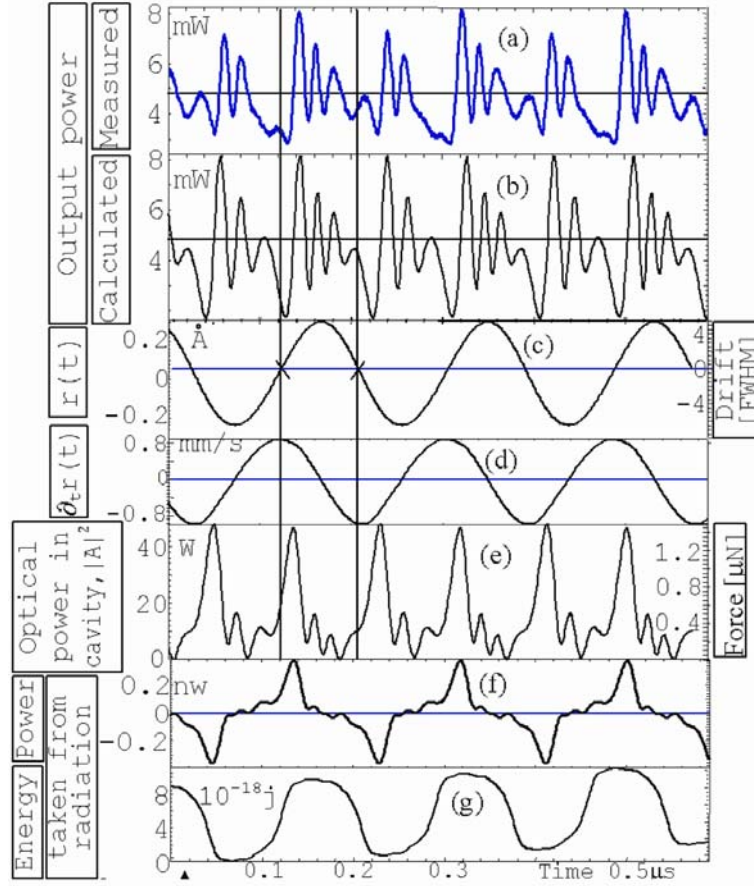


Figure 5.6: Plots versus time of (a) measured and (b) calculated transmitted optical power; (c) cavity displacement (d); velocity; (e) optical power circulating in cavity (left ordinate), which is proportional to the total radial force (right ordinate) applied by radiation on the cavity; (f) power flow to mechanical mode; and (g) energy transferred to mechanical mode from radiation. Here, the toroid radius is $R = 29 \mu\text{m}$, the mass was calculated (from SEM imaging) to be $5 \times 10^{-11} \text{Kg}$, the intrinsic mechanical quality factor was measured to be 1200, and the mechanical oscillation frequency occurs at 5.4 MHz. The pump power frequency is fixed at detuning of 0.55 FWHM away from the cavity optical resonance ($\lambda_0 = 1461 \text{nm}$), and the optical quality factor was measured to be $Q_o = 5 \times 10^7$.

5-5 Experimental Study of Below and Above Threshold Behavior

In order to verify the predictions of the above findings in the *sub-threshold regime*, the mechanical damping rate was measured as a function of optical pump power. In this regime, damping of mechanical oscillations can be decreased by injecting optical power into the microtoroid, yet the induced mechanical gain is not sufficient to initiate the regenerative vibrations. To measure the damping rate, an optical pump and probe approach was used (similar to Kerr-nonlinearity measurement in chapter 4) with two laser beams (a strong pump and a weak probe) individually resonant with two whispering gallery mode optical resonances. The experimental setup is depicted in Figure 5.7.

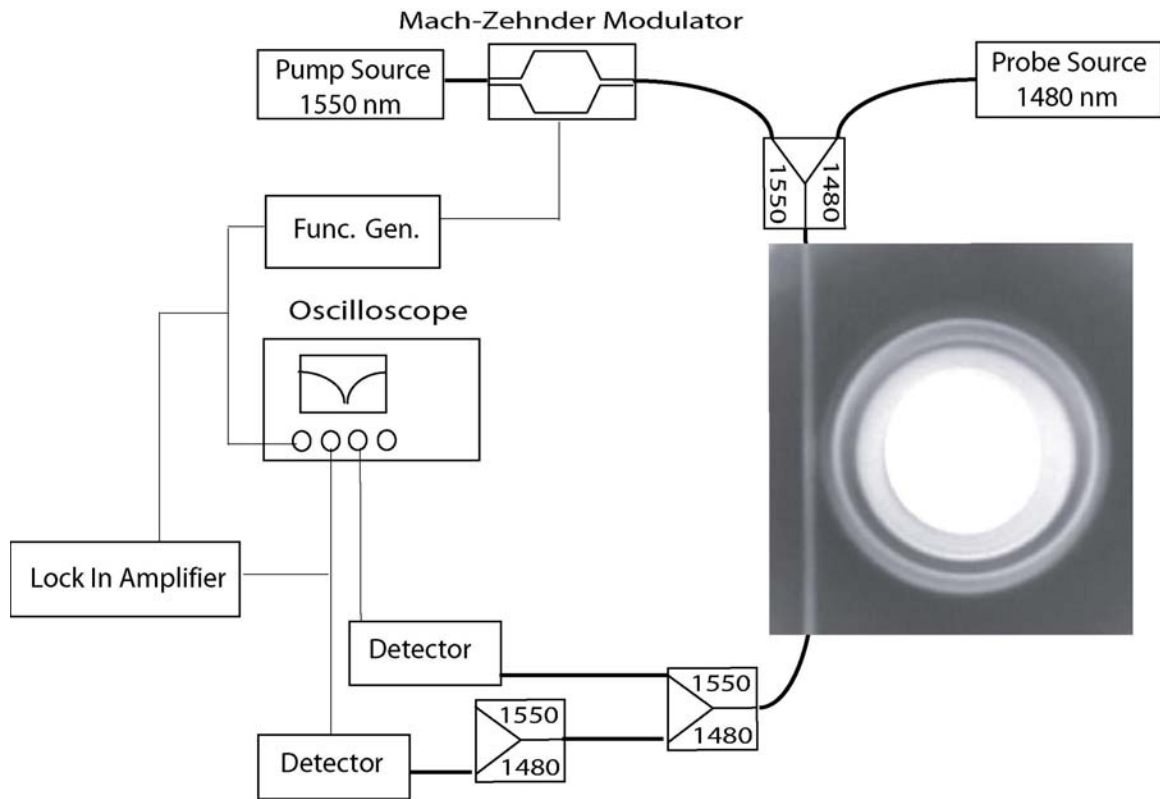


Figure 5.7: The experimental setup used for characterizing the mechanical oscillations of microtoroids in the subthreshold regime. Two wavelength couplers are used to ensure high extinction of the pump power in the probe channel. The picture is a top-view optical micrograph of a toroid microresonator evanescently side coupled to a tapered optical fiber.

Two, external-cavity diode lasers with 300 kHz linewidth were used as laser sources. The pump laser in the 1550 nm band and probe laser in the 1480 nm band were coupled to the microcavity using a tapered optical [27]. The output of the 1550 nm laser was weakly modulated using a Mach-Zehnder modulator. In this way the “DC” component of the pump power creates gain for the mechanical modes while the alternating component creates a harmonically-varying radiation-pressure that acts as a forcing function on the sub-threshold vibrational modes. Since the response motion also causes frequency shifts of the optical mode that is resonant with the probe signal, the mechanical response as a function of forcing-function frequency can be measured using the optical probe wave. The resulting modulation of the probe power can be measured using a lock-in amplifier, and it can be related to the amplitude of vibrations by measuring the quality factor of the optical mode coupled to the probe wave and its detuning from probe signal (for these experiments the weak probe beam was coupled to a low Q ($\sim 10^6$) whispering gallery resonance to ensure that probe power would not induce a competing oscillation effect). In this way, “vibrational spectroscopy” can be performed by sweeping the modulation frequency through the vibrational resonances. This spectroscopy reveals the lineshape of the mechanical resonance and hence its linewidth (and damping rate or equivalently the mechanical Q factor). Figure 5.8 gives sample spectroscopic scans over an $n=1$ vibrational mode with a resonant frequency of 7.67 MHz. The solid lines are the theoretical fits using a damped harmonic oscillator model for the mechanical motion. The inset in Figure 5.8 gives measured damping rates (extracted from the theoretical fits like that shown in the main Figure) plotted versus optical pump power using the pump/probe spectroscopy measurements. A linear decrease

in damping with increasing pump power is evident in the data (in agreement with equation 5.4). Also apparent is the threshold power, which in this case is expected to occur at an optical pump power of 11 micro Watts. The intrinsic Q factor of the mechanical mode (i.e., Q factor at zero input pump power) is inferred to be 630 in this data.

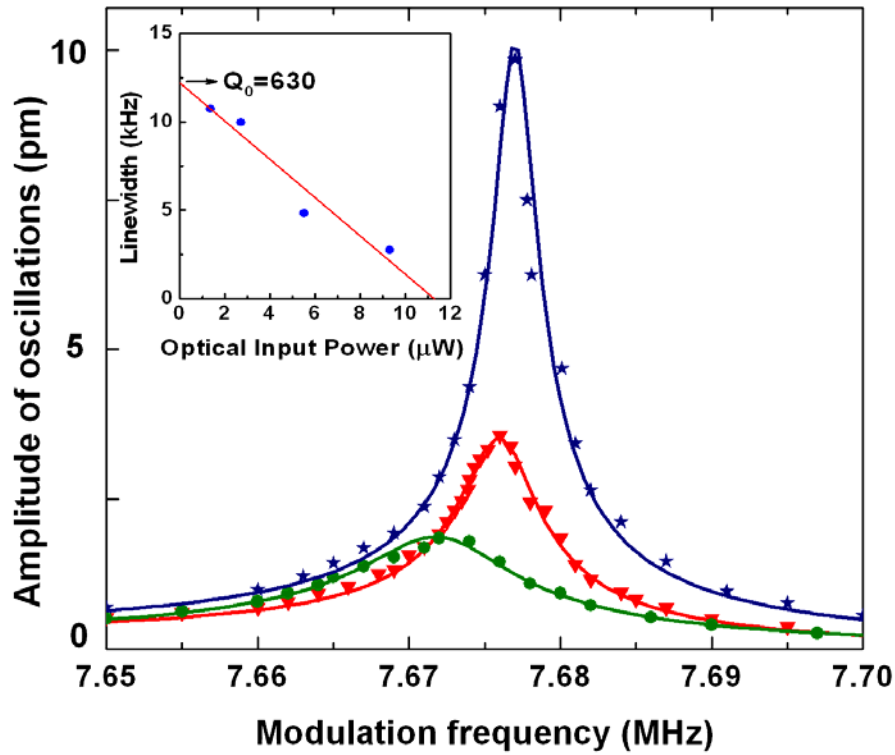


Figure 5.8: Measured amplitude response (points) of the mechanical vibrations of an $n=1$ mechanical mode as a function of driving-force frequency (modulation frequency of the pump power). Circles (green), triangles (red), and stars (blue) represent the data for $2 \mu W$, $5 \mu W$, and $9 \mu W$ of average pump power. The inset shows the effect of the optical power on the linewidth of the mechanical oscillator inferred from the theoretical fits (such as the solid lines in the main Figure). A linear fit shows a threshold of $11 \mu W$ for the mechanical oscillations and an intrinsic quality factor of 630 for the measured mechanical mode of the toroidal structure.

To characterize the mechanical modes in the above-threshold regime, the weak modulation of the pump power was terminated (i.e., steady pump wave) and the spectral content of the transmitted probe power was analyzed to monitor regenerative mechanical oscillations. The Fourier component of the transmitted probe power at the mechanical resonant frequency (Ω) was monitored by the electrical spectrum analyzer. The intensity of this signal, proportional to the amplitude of the vibrations caused by the pump wave, was measured as a function of pump power. Figure 9 contains a typical result of these measurements for one of the studied devices and shows a clear threshold for the vibrational oscillations. Since the oscillator behaves as an optical power modulator [21] the electrical spectrum analyzer data can be transformed to compute the actual amplitude of mechanical motion. More precisely, modulation depth in the optical power can be transformed into frequency variation caused by the mechanical motion using the measured linewidth of the optical mode. This frequency variation, however, is directly proportional to the ratio of amplitude of the mechanical motion to the radius of the microtoroid. This transformation has been used to calibrate the vertical axis in Figure 9. The data in Figure 9 also seem to suggest that the amplitude of the vibrations saturates at high pump powers. Numerical modeling shows that this behavior can be attributed to the induced frequency shifts of the cavity that, for higher pump power levels, exceed the cavity linewidth. This, in turn, reduces the efficacy of the pumping mechanism as the pump wave spends a progressively smaller fraction of time on resonance during each mechanical cycle [28].

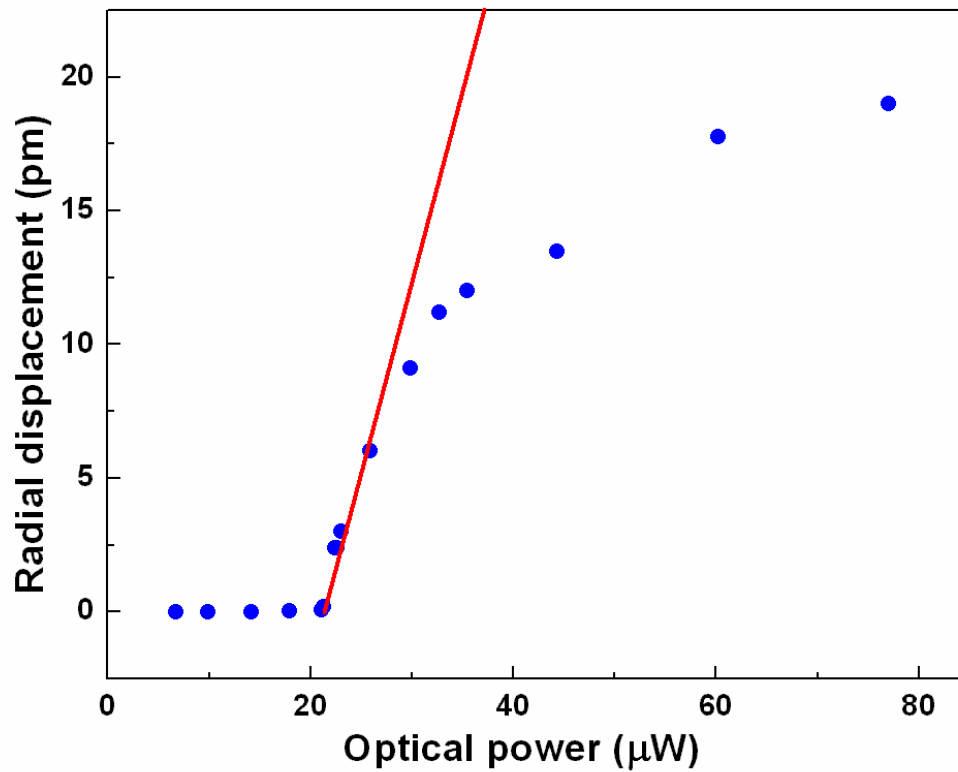


Figure 5.9: Measured mechanical oscillator displacement as a function of the optical pump power showing threshold behavior. Oscillations initiate at about $20 \mu W$ of input power and start to saturate for higher values of pump power. This saturation is associated with the lower optical-mechanical coupling at displacements large enough to shift the resonant frequency of the optical mode by greater than its linewidth.

5-6 Beyond Adiabatic Approximation: Coupled Mode Theory of Parametric Instability

In the theoretical work of Braginsky [1,2] it was shown that the interaction of the vibrating resonator (at frequency Ω) with photons inside the cavity results in the creation of photons down-shifted (Stokes sideband, $\omega - \Omega$) or up-shifted (anti-Stokes sideband, $\omega + \Omega$) in energy from the original photons by the frequency of the vibrations. If the Stokes field coincides with an adjacent optical resonance (Figure 5.10a), beating of the pump and Stokes-sideband provides mechanical gain for regenerative mechanical oscillations, thereby causing the parametric oscillation instability.

It is important to note that optical resonances with Q-factors in the 10^6 - 10^8 range have resonant linewidths in the range of ca. 2-200 MHz in the infra-red frequencies, which is indeed the range of the first three fundamental flexural modes for typical toroidal geometries employed in this work. This insight suggests that in addition to the Braginsky's theory [1], where the Stokes mode must coincide with an adjacent optical mode, mechanical oscillations can also occur when the mechanical resonance frequencies (Ω) fall within the same cavity bandwidth (ω/Q_{tot}) [29] of the pump mode (i.e., $\Omega \approx \omega/Q_{tot}$), heretofore called the “in-band” case (Figure 5.10b).

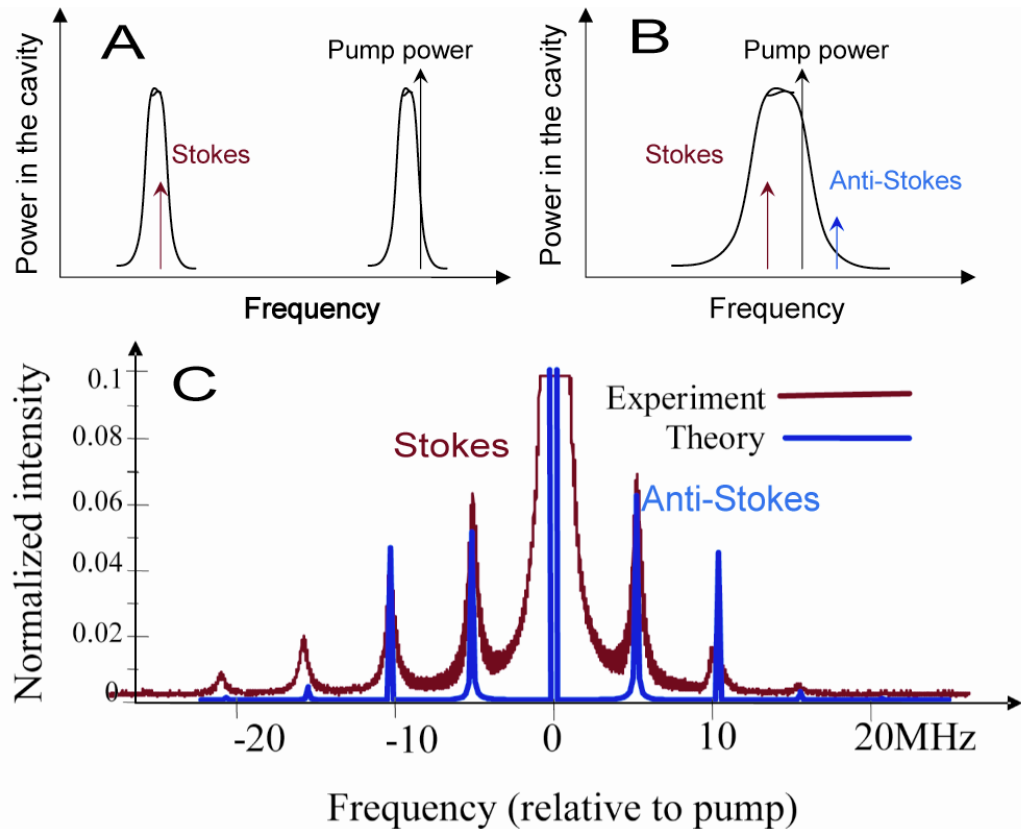


Figure 5.10: Panel A: represents Braginsky's view of parametric instability in the frequency domain, where the Stokes side band coincides with an adjacent optical mode. Panel B: shows the scenario we have encountered in our observations where the Stokes and anti-Stokes side bands both fall almost within the bandwidth of the same optical mode. Panel C: the experimental demonstration of the panel B scenario. Optical power out-coupled from a toroid microcavity oscillating at about 5 MHz frequency is measured by a 1MHz-resolution spectrum analyzer (high finesse Fabry-Perot). Higher optical side bands exist due to interaction of the Stokes and anti Stokes side bands with the mechanical mode. Theoretical predictions are also given.

The adiabatic regime, for example, $\Omega \ll \omega/Q_{tot}$ (see section 5.4), is in fact a special case of the in-band parametric instability ($\Omega \approx \omega/Q_{tot}$), where Braginsky's "out of band" picture does not hold. The adiabatic approach has to be modified, however, to predict correct threshold powers where the mechanical frequency is comparable to or even larger than the optical resonant linewidths (which are also observed in our studies), but is still too small to generate side-bands coinciding with an adjacent optical mode (see Figure 5.10a,b). To arrive at an analytical expression for the threshold power in these cases we have extended the theory of Braginsky for a Fabry-Perot cavity [1]. Using the slowly varying envelope approximation and the formalism of H. Haus, the mutual coupling of mechanical and optical modes can be described by:

$$\begin{aligned} \frac{d}{dt} x_m &= -\frac{\Omega}{2Q_m} x_m - \frac{i}{2Rn_{eff}\sqrt{m_{eff}}} C(\Gamma) e^{i\Omega t} \cdot |a|^2 \\ \frac{d}{dt} a &= -\frac{\omega_0}{2Q_{tot}} a + [i\Delta\omega + \frac{i\omega_0}{R\Omega\sqrt{m_{eff}}} e^{i\Omega t} x_m] a + i\sqrt{\frac{\omega_0}{Q_{tot}}} B \end{aligned} \quad (5.5)$$

These equations are identical to equations (5.1-5.3). The first equation describes the mechanical eigenmode with an effective mass m_{eff} , where x_m (as opposed to x , which represents the radial motion of the cavity used in equations 5.1-5.3) is normalized to mechanical energy, i.e., $|x_m|^2 = \sum_{i=r,z,\theta} \int \varepsilon_i \sigma_i dV$, (σ_i and ε_i are the diagonal components of the stress and strain tensor) which decays with the lifetime $\frac{Q_m}{\Omega}$. $C(\Gamma)$ is a correction factor [1...2] due to the reduction of circulating power in the presence of modal coupling [30]. Correspondingly $|a|^2$ is the energy in the optical WGM mode (as opposed to $|A(t)|^2$

used earlier to denote the optical power in the cavity), which is excited with a pump laser (with power $|B|^2$) detuned by the amount $\Delta\omega$ from line-center, $\Delta\omega = \omega - \omega_o$.

Assuming the optical field in the cavity is composed of the pump and the generated Stokes and anti-Stokes fields with corresponding detunings $\Delta\omega$, $\Delta\omega_S = \Delta\omega - \Omega$ and $\Delta\omega_{AS} = \Delta\omega + \Omega$ from cavity line-center ω_o (i.e., $a e^{i\Delta\omega t} = a_p e^{i\Delta\omega t} + a_S e^{i\Delta\omega_S t} + a_{AS} e^{i\Delta\omega_{AS} t}$), equation 5.5 results in four coupled mode equations:

$$\begin{aligned}
\frac{\partial x_m}{\partial t} &= -\frac{\Omega}{2Q_m} x_m + \frac{-i}{2Rn_{eff} \sqrt{m_{eff}} C(\Gamma)} (a_p^* a_{AS} + a_p a_S^*), \\
\frac{\partial a_p}{\partial t} &= -\frac{\omega}{2Q_{tot}} a_p + i\Delta\omega a_p + \frac{i\omega}{R\sqrt{m_{eff}} \Omega} (x_m^* a_{AS} + x_m a_S) + i\sqrt{\frac{\omega}{Q_{ext}}} B, \\
\frac{\partial a_S^*}{\partial t} &= -\frac{\omega}{2Q_{tot}} a_S^* - i(\Delta\omega - \Omega) a_S^* - \frac{i\omega}{R\sqrt{m_{eff}} \Omega} x_m a_p^*, \\
\frac{\partial a_{AS}}{\partial t} &= -\frac{\omega}{2Q_{tot}} a_{AS} + i(\Delta\omega + \Omega) a_{AS} + \frac{i\omega}{R\sqrt{m_{eff}} \Omega} x_m a_p.
\end{aligned} \tag{5.6}$$

Solving these equations in steady state yields the threshold for radiation pressure induced mechanical oscillation:

$$P_{thresh} = R^2 m_{eff} \frac{\omega_o}{Q_0 Q_{tot}} \frac{\Omega^2}{Q_m} \frac{|1 + K + 2iQ_0 \Delta\omega / \omega_o|^2}{8K} \times \left[\frac{1}{1 + 4 \left(\frac{Q_{tot} \Delta\omega_{AS}}{\omega_o} \right)^2} - \frac{1}{1 + 4 \left(\frac{Q_{tot} \Delta\omega_S}{\omega_o} \right)^2} \right]^{-1} \tag{5.7}$$

The threshold equation reveals that in order to arrive at oscillation, the mechanical loss has to be overcome (i.e., the expected $1/Q_m$ dependence). Dependence of radiation pressure upon circulating optical power, however, leads to the $1/Q_0$ dependence as well as the presence of a weighting factor describing the effect of waveguide coupling,

$K = \frac{Q_o}{Q_{ex}}$ [30]. The last term results from the interplay of the Stokes and anti-Stokes

photons, which provide mechanical gain and loss, respectively. Figure 5.11 shows a plot of the mechanical gain (inverse of equation 5.7) as a function of both coupling (K) and detuning frequency ($\Delta\omega$) for the n=1 and n=3 mechanical modes, which will be predominantly analyzed in the experiments. It is noted, that the mechanical gain is only positive for a blue detuned pump with respect to the cavity resonance $\Delta\omega > 0$. This situation leads to more Stokes than anti-Stokes photons (the ratio

being $\left| \frac{a_{AS}}{a_S} \right|^2 = \frac{(\omega_0 / Q_{tot})^2 + 4(\Delta\omega_S)^2}{(\omega_0 / Q_{tot})^2 + 4(\Delta\omega_{AS})^2}$) and causes a net mechanical gain. The converse is

true for red-detuned pump, which causes the mechanical resonance to experience negative gain (i.e., damping). For the special case of $\Delta\omega = 0$, the gain vanishes. These are all in agreement with our findings in the adiabatic regime (see equation 5.4 and definition of d factor).

Furthermore, it is interesting to investigate the exact Q-factor dependence of threshold power shown in the inset of Figure 5.11. As expected, in the adiabatic regime,

$\Omega \ll \omega / Q_{tot}$, the mechanical oscillation threshold power scales as $P_{thresh} \propto \frac{1}{Q_m} \cdot \left(\frac{1}{Q_0} \right)^3$

in agreement with our previous expression for this regime (the reader can verify that in this regime the expression for threshold power reduces exactly to equation 5.4). In contrast, if the mechanical eigenfrequencies lie outside the cavity band-width, i.e.,

$\Omega > \omega / Q_{tot}$, the threshold scales as $P_{thresh} \propto \frac{1}{\Omega^2 Q_m} \cdot \frac{\Delta\omega}{\omega_0}$, causing a roll-off of the

optical Q dependence. In fact, analysis of equation 5.7 shows that the minimum threshold

($\frac{\partial P_{thresh}}{\partial K \partial \Delta \omega} = 0$) for higher optical Q factors, approaches asymptotically a limiting value,

which can only be achieved for progressively stronger over-coupling (and correspondingly increasing the cavity bandwidth until the condition $\omega / Q_{tot} \approx \Omega$ is met).

The roll-over from inverse-cubic behavior occurs when $\frac{\omega_0}{Q_0} \propto \Omega$, i.e., $Q_0^{roll-over} \cong \frac{\omega_0}{\Omega}$ as

observed in the inset of Figure 5.11.

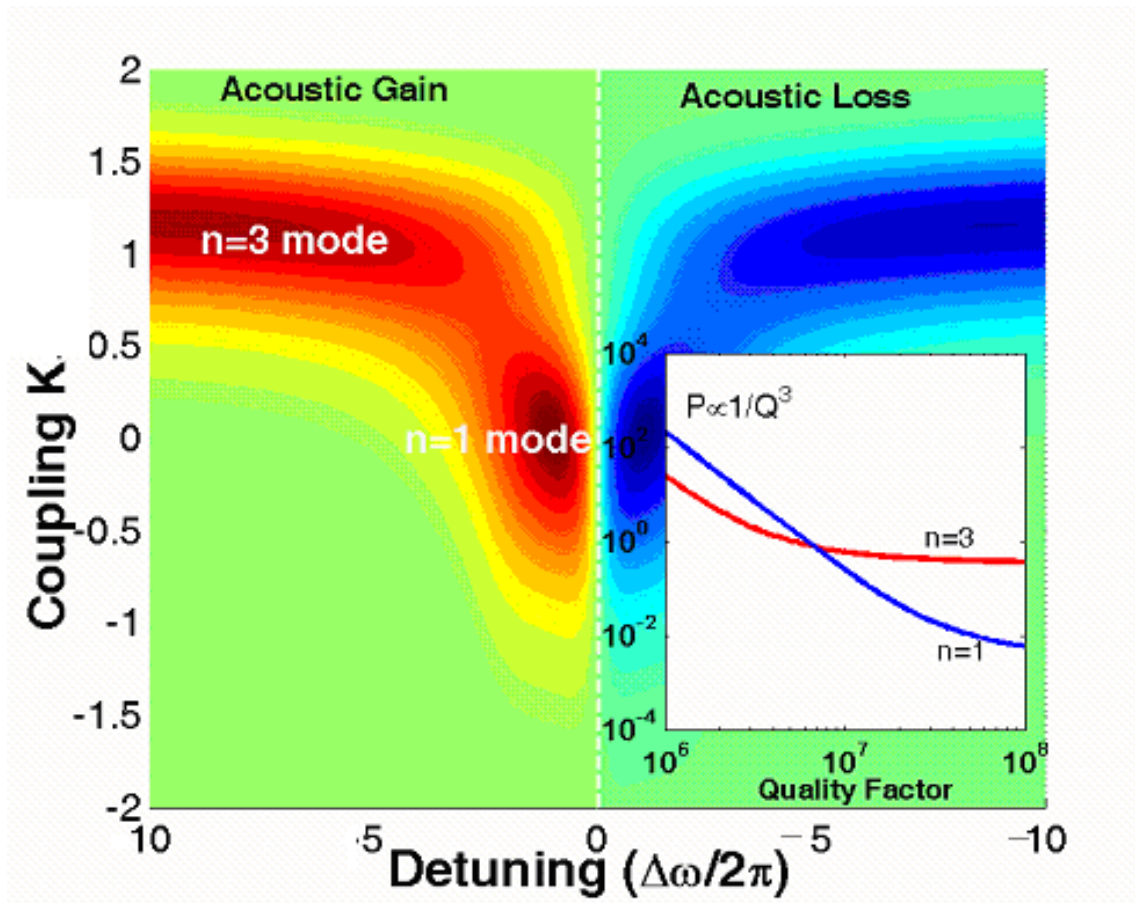


Figure 5.11: Mechanical gain (from equation 5.7) as a function of detuning (negative detuning corresponds to a redshift) and taper-waveguide-cavity coupling (simulation parameters $\nu_1=4.4$ MHz, $\nu_3=49.8$ MHz, $Q_0=5 \times 10^7$). Maximum gain for the $n=1$ mode occurs in the under-coupled regime ($\log(K)<0$), whereas for the $n=3$ mode it occurs overcoupled ($\log(K)>0$). Inset: Double logarithmic plot of the *minimum* oscillation threshold power for the $n=1$ and $n=3$ mode (equation 5.7) versus the intrinsic optical quality factor.

5-7 Experimental Investigation of Parametric Instability Threshold

Power

In order to confirm the threshold dependence (as given by equation 5.7) on both optical and mechanical Q-factors we have carried out numerous experiments and simulations on a single toroid microresonator. The microtoroid under consideration had principal, pillar, and toroid diameter of 72 μm , 36 μm , and 6.8 μm and possessed mechanical resonance frequencies at (4.4 MHz, 25.6 MHz, and 49.8 MHz) for the first three modes ($n=1,2,3$ and $m=0$). Minimum threshold power was measured by optimizing the detuning and coupling (compare Figure 5.11). The result of this measurement is shown in Figure 5.12. A double logarithmic plot is used to infer the critical exponent, which shows excellent agreement with the prediction ($1/Q^3$) for adiabatic regime. For progressively higher Q values, the theoretically predicted roll-over of the $1/Q^3$ threshold dependence is observed. The roll-over point occurs at a Q of ca. 10^7 , which agrees well with the prediction

$Q_0^{\text{roll-over}} = \frac{\omega_0}{\Omega}$ for the first-order flexural mode. The solid line is the minimum threshold

as given by equation (5.7), which is minimized with respect to detuning ($\Delta\omega$) and

coupling (K) to reflect the experiments, i.e., $\frac{\partial P_{\text{thresh}}}{\partial K \partial \Delta\omega} = 0$. The effective mass was the *only*

fit parameter used and was inferred to be ($m_{\text{eff}}^{(1)} \approx 3.3 \times 10^{-8} \text{ Kg}$).

The threshold for the 3rd order flexural mode was also recorded. This mode has a resonance frequency of 49.8 MHz with $Q_m^{n=3} \approx 2500$. Consequently for optical Q factors in the range of 10^7 this mode is in the beyond-cavity-bandwidth regime,

since $Q_0^{\text{roll-over}} = \frac{\omega_0}{\Omega} = 4 \times 10^6$. In the experiments, oscillation on this high frequency mode

was only observed by adjusting the taper-resonator coupling junction into the over-coupled regime, in agreement with theory. In this regime the low frequency flexural mode could not be excited any more, and a transition from $n=1$ to $n=3$ occurred. This transition is in excellent agreement with the theoretical prediction of equation 5.7, as plotted in Figure 5.11. The inset of Figure 5.12 shows the measured threshold for the $n=3$ resonance in comparison with the $n=1$ mode. The single parameter fit yields an effective mass for the $n = 3$ mode, which is significantly lower than for $n=1$, by a factor of 660, i.e., $m_{eff}^{(3)} \approx 5 \times 10^{-11} \text{ Kg}$. Note, that the reason for yet lower threshold values of the $n=1$ mode, lies in the fact that the $n=3$ mode is in the beyond-cavity-bandwidth regime for the Q-values $>10^7$ (where the roll-over behavior happens in the optical Q dependence). However, for lower Q, the $n=3$ mode has indeed lower threshold, and the crossing of $n = 1$ and $n = 3$ has indeed been observed in experiments (compare with the inset of Figure 5.10).

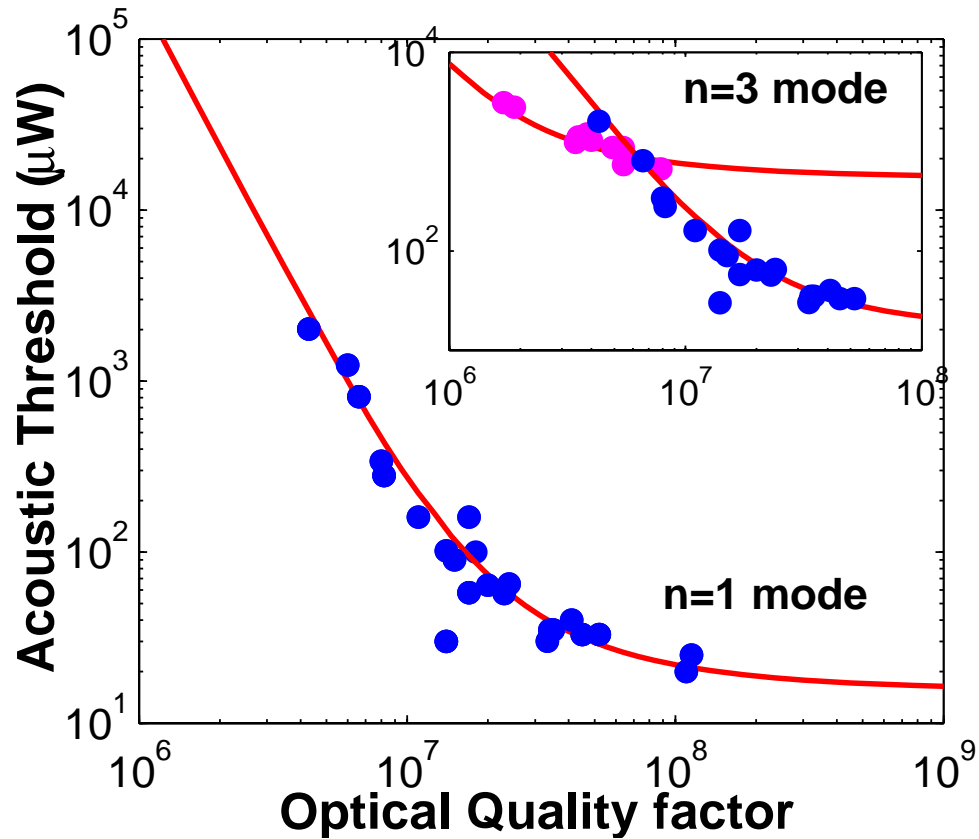


Figure 5.12: Main panel: The measured mechanical oscillation threshold (in μ Watts) plotted versus the optical quality factor for the fundamental flexural mode ($n=1, \Omega/2\pi = 4.4\text{MHz}, Q_m = 3500$) on a double logarithmic scale. The solid line is a one-parameter theoretical fit obtained from the minimum threshold equation by first performing a minimization with respect to coupling and pump wave detuning, and then fitting by adjustment of the effective mass ($m_{\text{eff}}^{(1)} \approx 3.3 \times 10^{-8} \text{Kg}$). Inset shows the measured threshold for the 3rd order mode ($n=3, \Omega/2\pi = 49.8\text{MHz}, Q_m = 2500$) plotted versus optical Q. The solid line gives again the theoretical prediction with $m_{\text{eff}}^{(3)} \approx 5 \times 10^{-11} \text{Kg}$. The $n=1$ mode data from the main Figure is superimposed for comparison.

The mechanical eigenmodes of microtoroids can be considered as a combination of two harmonic oscillators: within-plane oscillator (radial amplitude x , which modulates the cavity path length) and out-of-plane oscillator (amplitude z , which does not affect the optical path length). Note that the mechanical energy E_m is also associated with both a radial motion ($m_{eff}\Omega^2x^2$) and a transverse motion. Since only the radial direction modulates the cavity path-length (with amplitude x), the effective mass m_{eff} for the radial motion is given by:

$$m_{eff} \equiv \frac{E_m}{\Omega^2 x^2} = \frac{1}{\Omega^2 x^2} \left(\sum_{i=x,z,\theta} \int \varepsilon_i \sigma_i dV \right) \quad (5.8)$$

and can be evaluated by finite element simulation. The effective mass in the radial direction will always be higher than the total mass of the structure, since not all motion is occurring in the radial direction.

For the $n = 3$ mode, the predicted effective mass from our numerical models associated with the radial motion was $m_{eff}^{(3)} \approx 5 \times 10^{-11} \text{ Kg}$, which is in very good agreement with the experimental fit in Figure 5.12. Furthermore, this value is exceptionally close to the actual mass of the vibrating structure. This can be intuitively expected as the $n=3$ motion is primarily radial (see Figure 5.4) and therefore the out-of-plane motion and its contribution to the mechanical energy is negligible.

For the $n=1, 2$ modes, however, the calculated effective mass is a strong function of the offset of the toroidal ring with respect to the equatorial plane of the disk [31]. As explained in section 5-3, excitation of the $n=1$ mode by radiation pressure can only be explained by existence of this offset. To both validate and quantify this offset, a cross section of the toroid microcavity used in the study was obtained with focused-ion beam

slicing. SEM imaging included in Figure 5.13 reveals the presence of the above postulated equatorial offset, which amounts to an offset of $1.3 \mu m$. Incorporation of this offset to the numerical mass calculations yields $m_{eff}^{(1)} \approx 2.6 \times 10^{-8} Kg$ and $m_{eff}^{(2)} \approx 2 \times 10^{-9} Kg$. This value agrees very well with the experimental values from Figure 5.12. Finally, the numerical model also explains why the n=2 mode is observed only subthreshold in the experiments. The low mechanical Q value (~ 200), in conjunction with its high effective mass and frequency, predicts threshold powers greater than 2mW.

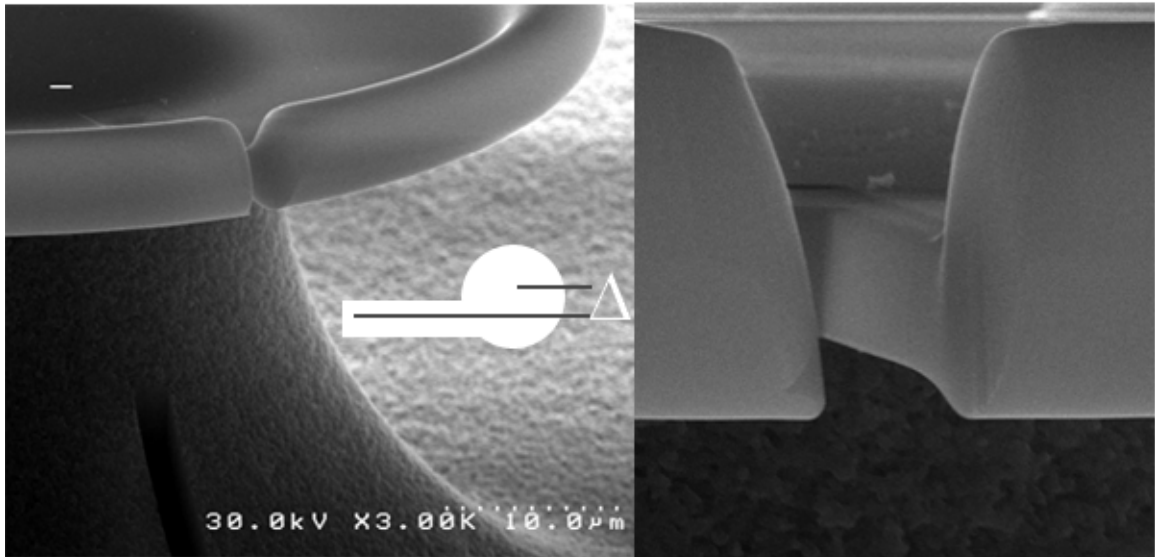


Figure 5.13: Scanning-electron micrograph of a cross section of the toroid microcavity used in this study. The cross section was revealed by focused-ion beam (FIB) technology, which allowed removal of a 2 micron wide section. The slicing clearly reveals the presence of an offset of the 7-micron-diameter toroid with respect to the 2-micron thick silica support disk (in this case an offset of ca 1.3 micron, dotted lines). Inset: side view of the toroid microcavity inferred from the FIB method.

We next proceeded to verify the dependence of threshold power on the mechanical quality factor. As both optical and mechanical Q affect threshold, a method was needed that could reduce the mechanical Q factor while leaving the optical Q factor unchanged. To this end, we used a silica-microprobe fabricated by heating and stretching a single-mode-fiber using a CO₂ laser. An optical micrograph is shown in the inset of Figure 5.14 where the mechanical probe is mounted on a 3-axis piezoelectric stack and positioned above the fiber-taper coupled microtoroid. When the probe was brought into contact with parts of the microstructure exhibiting high-amplitude mechanical oscillations (compare the mode profiles in Figure 5.4) a reduction of the mechanical Q-factor was observed, while leaving the optical Q-factor unaffected. The change in mechanical Q-factor was measured by fitting the ESA-measured resonances in the sub-threshold regime with Lorentzian profiles. Without contact the mechanical Q was measured to be ~5000 for the n=1 mode, and upon progressive increase in tip pressure (controlled via piezo-electric distance) the mechanical Q could be continuously decreased by nearly two orders of magnitude, down to a value of 50. Upon retrieving the probe the original Q-factor was recovered. The microprobe method thus allowed changing the mechanical Q, while leaving the optical modes unperturbed. For each mechanical Q the minimum threshold for the n=1 flexural mode (by optimizing both $\Delta\omega$ and K) was measured. Figure 5.14 shows the measured minimum threshold for oscillation of n=1 mode as a function of mechanical Q-factor, clearly revealing the $1/Q_m$ dependence of the oscillation threshold, in agreement with equations 5.4 and 5.7, as well as theoretical predictions of Braginsky [32,33]. This method also provides a technique to prevent parametric oscillation instability for cases where this effect is not desirable.

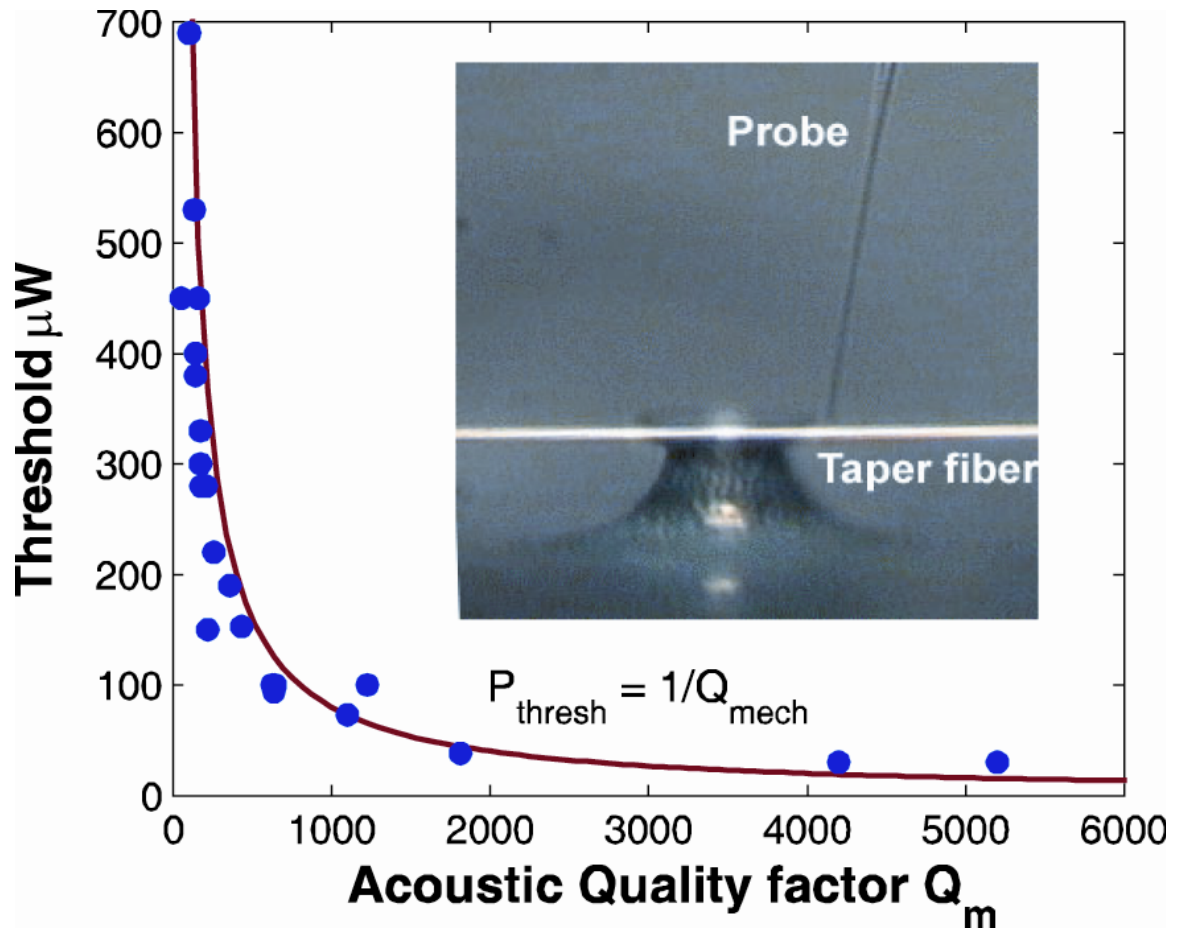


Figure 5.14: The mechanical threshold power (in micro Watts) versus the mechanical quality factor of the $n=1$ mode. The solid line is the theoretical prediction ($P_{\text{thresh}} \propto 1/Q_m$). Inset: Optical micrograph of the side view of the experimental setup, consisting of a silica microprobe in proximity of a fiber-coupled microtoroid of 72-micron-principal diameter.

5-8 Conclusions

The work presented in this chapter is the first demonstration of the radiation-pressure-induced parametric instability in optical resonators of any kind. This work demonstrates how vibrational and optical modes of the same cavity structure can act as parametrically coupled oscillators despite their very different frequencies ($\sim 10^7$ against $\sim 10^{14}$ Hz). Realization of this effect in microscale can be utilized as a platform for studying the parametric-instability limitations for LIGO project.

It should be noted that mechanical oscillations in microstructures can be generated using alternative methods. For example, references [34,35] describe thermally actuated mechanical vibrations of a silicon disk and a silicon cantilever, respectively. In contrast, the long thermal time constant of the toroidal structures in the present work ($\tau_{thermal}$ is in the order of $5\mu s$ [36,37]) precludes initiation of RF rate oscillations such as those observed here. Also significant is the expected threshold dependence on optical Q for thermally driven instabilities. Because resonator deformation for a thermally driven process (as opposed to radiation pressure) depends on coupled optical power (not circulating power) one expects an inverse quadratic scaling of the threshold power with optical Q ($P_{threshold} \propto Q^{-2}$) for thermally induced oscillations as opposed to inverse cubic ($P_{threshold} \propto Q^{-3}$) for radiation pressure-induced-oscillations verified in this study. Excellent agreement of the threshold functional dependence on optical and mechanical Q factors, and precise numerical predictions of the threshold power, provides confirmation that radiation pressure *is* the excitation mechanism of the observed oscillations.

In small microtoroids (we were also able to observe similar oscillations in silica microspheres), occurrence of these oscillations has been observed with threshold powers

well below those of other nonlinear effects such as Raman [38,39], Kerr parametric oscillation [40], and lasing due to intentional doping of rare-earth elements into the microcavities [41]. This clearly suggests that radiation-pressure-induced effects can establish a practical limit for miniaturization of optical microcavities. This miniaturization limit can be extended by adding a mechanical damper (or displacement limiter as in Figure 5.14) to the cavity structure. Yet, the fundamental nature of circulating light to apply pressure and the general nature of structural stiffness to reduce with miniaturization [42] suggest that it is likely that all optical cavities are susceptible to these oscillations at various optical powers. The inverse cubic dependence of threshold power suggests that current efforts directed towards realization of higher Q optical microcavities will only tend to accelerate the observation of these oscillations in other microcavity systems either as a limiting floor in miniaturization, or as a useful new optomechanical nonlinearity.

Beyond limitations caused by radiation-pressure-induced optomechanical coupling, the parametric instability demonstrates a new class of hybrid oscillators where a continuous source of pump-laser power (without any type of external feedback system) can generate radio frequency mechanical vibrations of a micromechanical structure (a rendering of the oscillation process for the $n=3$ mode is shown in Figure 5.15). These oscillations imprint onto the optical pump, now an optical carrier for RF frequencies. Realization of this effect undoubtedly benefits applications in RF micromechanical oscillators [43] on a chip and all-optical frequency reference devices.

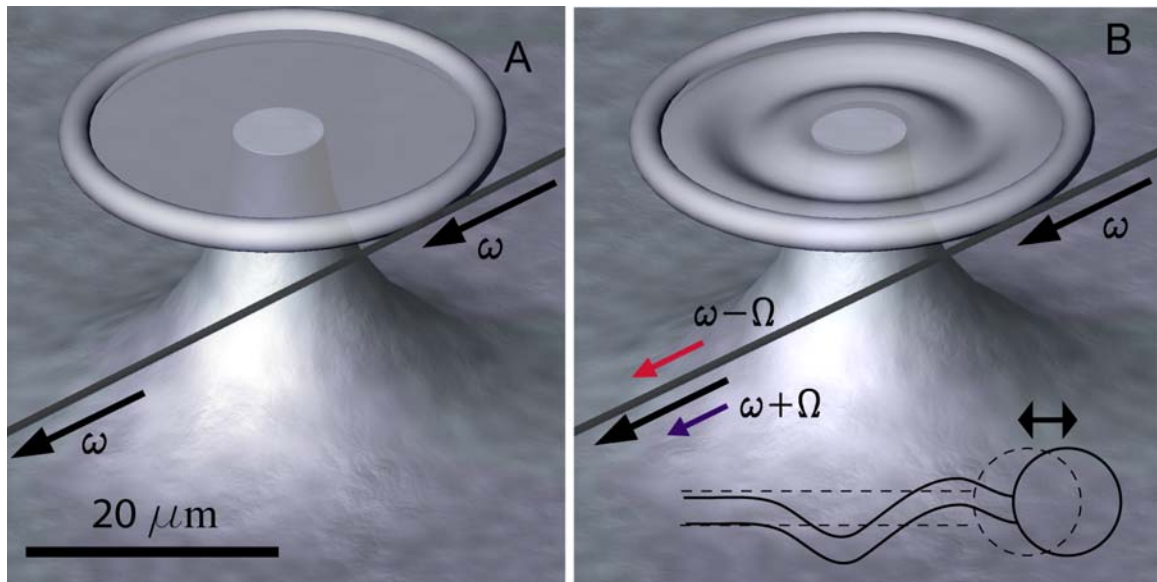


Figure 5.15: Panel A illustrates the “below threshold” behavior where the optical pump wave at frequency ω is not strong enough to induce mechanical oscillations of the microtoroid. Panel B illustrates the “above threshold” case for the $n=3$ vibrational mode. Mechanical oscillation at frequency Ω creates optical stokes ($\omega - \Omega$) and anti-stokes ($\omega + \Omega$) sidebands in the transmitted pump wave. Inset of panel B shows the exaggerated cross-section of the third-order eigenmode and variation of the toroid radius as a result of these oscillations.

Besides the fundamental aspects of this work, the observed coupling of mechanical and optical modes by radiation pressure can find applications in micromechanical and nanomechanical systems [44] for ultra-high sensitivity measurements of charge [45], displacement, mass, force [46], or biological entities [47]. Equally important, radiation pressure as observed here can be used to achieve cooling of mechanical resonator modes [35].

We believe the promising consequences of our recent research results will pave the way for further practical applications of UHQ microcavities and introduce them to an exciting and drastically novel realm of science.

5-9 Bibliography

- [1] V. B. Braginsky, S. E. Strigin, and S. P. Vyatchanin. Parametric oscillatory instability in Fabry-Perot interferometer. *Physics Letters A*, vol. 287(5-6): 331-338, 2001.
- [2] V. B. Braginsky, S. E. Strigin, and S. P. Vyatchanin. Analysis of parametric oscillatory instability in power recycled LIGO interferometer. *Physics Letters A*. 305(3-4): 111-124, 2002.
- [3] A. Abramovici *et al.* The Laser-Interferometer-Gravitational-Wave Observatory. *Science*, 256(5055): 325-333, 1992.
- [4] G. Amelino-Camelia. Gravity-wave interferometers as quantum-gravity detectors. *Nature*, 398(6724): 216-218, 1999.
- [5] W. Kells and E. D'Ambrosio. Considerations of parametric instability in Fabry Perot interferometer. *Physics Letters A*, 229(4): 326-330, 2002.
- [6] C. Zhao, L. Ju, J. Degallaix, S. Gras, D. G. Blair. Parametric instabilities and their control in advanced interferometer gravitational-wave detectors. *Physical Review Letters*, 94(12): art. no. 121102, 2005.
- [7] S. W. Schediwy, C. Zhao, L. Ju, *et al.* An experiment to investigate optical spring parametric instability. *Classical and Quantum Gravity*, 21(5): S1253-S12587, 2004.
- [8] A. Dorsel, J. D. McCullen, P. Meystre, E. Vignes, and H. Walther. Optical bistability and mirror confinement induced by radiation pressure. *Physical Review Letters*, 51(17): 1550-1553, 1983.
- [9] V. B. Braginsky, M. L. Gorodetsky, and V. S. Ilchenko. Quality-factor and nonlinear properties of optical whispering-gallery modes. *Physics Letters A*, 137(7-8): 393-397, 1989.

- [10] D. K. Armani, T. J. Kippenberg, S. M. Spillane, and K. J. Vahala. Ultra-high-Q toroid microcavity on a chip. *Nature*, 421(6926): 925-928, 2003.
- [11] L. Hilico, J. M. Courty, C. Fabre, *et al.* Squeezing with Chi (3) materials. *Applied Physics B-Photophysics and Laser Chemistry*, 55(3): 202-209, 1992.
- [12] V. Giovannetti, S. Mancini, and P. Tombesi. Radiation pressure induced Einstein-Podolsky-Rosen paradox. *Europhysics Letters* 54(5): 559-565, 2001.
- [13] S. Mancini, V. Giovanetti, D. Vitali, and P. Tombesi, “Entangling macroscopic oscillators exploiting radiation pressure,” *Phys. Rev. Lett.*, vol. 88, 120401, 2002.
- [14] S. Pirandola, S. Mancini, D. Vitali, and P. Tombesi. Continuous-variable entanglement and quantum-state teleportation between optical and macroscopic vibrational modes through radiation pressure. *Physical Review A.*, 68, art. no. 062317, 2003.
- [15] W. Marshall, C. Simon, R. Penrose, and D. Bouwmeester, Towards Quantum superpositions of a mirror. *Physical Review Letters*, 91, art. no. 130401, 2003.
- [16] S. Mancini, D. Vitali, and P. Tombesi. Scheme for teleportation of quantum states onto a mechanical resonator. *Physical Review Letters*, 90(13): art. no. 137901, 2003.
- [17] I. Tittonen, *et al.* Interferometric measurements of the position of a macroscopic body: Towards observation of quantum limits. *Physical Review A.*, 59(2): 1038-1044, 1999.
- [18] H. Rokhsari, T. J. Kippenberg, T. Carmon, and K. J. Vahala. Radiation-pressure-driven micromechanical oscillator. *Optics Express*, 13 (14): 523-5301, 2005.

- [19] T. J. Kippenberg, H. Rokhsari, T. Carmon, A. Scherer, and K. J. Vahala. Analysis of radiation-pressure induced mechanical oscillation of an optical microcavity. *Physical Review Letters*, 95(3): art. no. 033901, 2005.
- [20] T. Carmon, H. Rokhsari, L. Yang, T. J. Kippenberg, and K. J. Vahala. Temporal behavior of radiation-pressure-induced vibrations of an optical microcavity phonon mode. *Physical Review Letters*, 94(22): art. no. 223902, 2005.
- [21] The characteristics of the overall waveguide-resonator system can be viewed as an optical modulator that is driven by this oscillation. This modulator has a nonlinear transfer function that manifests itself (in the modulated pump power) through the appearance of harmonics of the characteristic mechanical eigenfrequencies. These harmonics are easily observed upon detection of the modulated pump (see Figure 5.3).
- [22] M. Cai, O. Painter and K. J. Vahala. Observation of critical coupling in a fiber taper to silica-microsphere whispering gallery mode system. *Physical Review Letters*, 85(1): 74-77, 2000.
- [23] From the simulations it is calculated that the change in refractive index due to the stress-optical effect is more than 1 order of magnitude smaller compared to the direct spatial change in cavity path length, i.e., $2\pi(R + dR) \times (\Delta n + n_{eff}) \approx 2\pi n_{eff} (R + dR)$.
- [24] R. M. Shelby, M. D. Levenson, and P. W. Bayer. Guided acoustic-wave Brillouin-scattering. *Physical Review B*, 31(8): 5244-5252, 1985.
- [25] M. L. Gorodetsky, and V. S. Ilchenko. Optical microsphere resonators: optimal coupling to high-Q whispering-gallery modes. *Journal of the Optical Society of America B-Optical Physics*, 16(1): 147-154, 1999.

- [26] For $f(d) < 0$, i.e., a red shift of the pump frequency with respect to the cavity mode, the phase of the radiation pressure variations actually damps or “cools” the vibrations. Note that no external feedback system is necessary here to damp the vibrations or “cool” the resonator. The feedback system is inherent to the coupling mechanism. Due to the high quality factor of our cavities ($Q \sim 10$ million) the “red-shifted” tail of the optical mode is not thermally stable (see H. Rokhsari *et. al.* Loss characterization in microcavities using the thermal bistability effect. *Applied Physics Letters*, 85(15): 3029-3031, 2004). Replacing the cavity material (silica) with a negative thermo-optic coefficient material would stabilize the red-shifted tail and cavity-cooling induced by radiation pressure effects could be observable.
- [27] S. M. Spillane, T. J. Kippenberg, O. J. Painter, and K. J. Vahala. Ideality in a fiber-taper-coupled microresonator system for application to cavity quantum electrodynamics. *Physical Review Letters*, 91(4): art. no. 043902, 2003.
- [28] For the sample tested, it is calculated that radial variations of about 10 picometers will shift the resonant frequency of the excited optical mode by its linewidth.
- [29] In special cases, we also observed the classical V. B. Braginsky case, which can occur since the WGM modes typically appear as doublets, due to the lifting of the CW and CCW mode degeneracy. If this doublet splitting coincides with the mechanical oscillation frequency, parametric oscillation instability can occur when pumping the blue-shifted doublet eigenmode, whereas it is absent on the red-shifted eigenmode.
- [30] T. J. Kippenberg, S. M. Spillane, and K. J. Vahal. Modal coupling in traveling-wave resonators. *Optics Letters*, 27(19): 1669-1673, 2002.

- [31] We note that such an offset must exist, since otherwise mechanical motion of the $n=1,2$ modes causes modulation of the path length at the frequency 2Ω (i.e., frequency doubling), which is not observed in experiments.
- [32] V. B. Braginsky, M. L. Gorodetsky, and V. S. Ilchenko. Quality-factor and nonlinear properties of optical whispering-gallery modes,” *Physics Letters A*, 137(7-8): 393-397, 1989.
- [33] V. B. Braginsky, M. L. Gorodetsky, V. S. Ilchenko, and S. P. Vyatchanin. On the ultimate sensitivity in coordinate measurements. *Physics Letters A*, 179(4-5): 244-248, 1993.
- [34] M. Zalalutdinov, *et al.* Autoparametric optical drive for micromechanical oscillators. *Applied Physics Letters*, 79(5): 695-697, 2001.
- [35] C. H. Metzger, and K. Karrai. Cavity cooling of a microlever. *Nature*, 432(7020): 1002-1005, 2004.
- [36] H. Rokhsari, S. M. Spillane, and K. J. Vahala. Observation of Kerr nonlinearity in microcavities at room temperature. *Optics Letters*, 30(4): 427-429, 2005.
- [37] V. S. Ilchenko, and M. L. Gorodetsky. Thermal nonlinear effects in optical whispering gallery microresonators. *Laser Physics*, 2: 1004-1009, 1992.
- [38] S. M. Spillane, T. J. Kippenberg, and K. J. Vahala. Ultralow-threshold Raman laser using a spherical dielectric microcavity. *Nature*, 415(6872): 621-623, 2002.
- [39] T. J. Kippenberg, S. M. Spillane, B. K. Min, and K. J. Vahala. Theoretical and experimental study of stimulated and cascaded Raman scattering in ultrahigh-Q optical microcavities. *IEEE Journal of Selected Topics in Quantum Electronics*, 10(5): 1219-1228, 2004.

- [40] T. J. Kippenberg, S. M. Spillane, and K. J. Vahala. Kerr-nonlinearity optical parametric oscillation in an ultrahigh-Q toroid microcavity. *Physical Review Letters*, 93(8): 083904, 2004.
- [41] L. Yang, D. K. Armani, and K. J. Vahala. Fiber-coupled Erbium microlasers on a chip. *Applied Physics Letters*, 83(5): 825-826, 2003.
- [42] The spring constant of a structure is proportional to its cross section area divided by its length and hence spring constant decreases with size.
- [43] X. M. H. Huang, C. A. Zorman, M. Mehregany, and M. L. Roukes. Nanodevice motion at microwave frequencies. *Nature*, 421(6922): 496-496, 2003.
- [44] H. G. Craighead. Nanoelectromechanical systems. *Science*, 290(5496): 1532-1535, 2000.
- [45] A. N. Cleland and M. L. Roukes. A nanometer-scale mechanical electrometer. *Nature*, 392(6672): 160-162, 1998.
- [46] D. Rugar, R. Budakian, H. J. Mamin, and B.W. Chui. Aingle spin detection by magnetic resonance force microscopy. *Nature*, 430(6997): 329-332, 2004.
- [47] B. Ilic, Y. Yang, and H. G. Craighead. Virus detection using nanoelectromechanical devices. *Applied Physics Letters*, 85(13):, 2604-2606, 2004.

Chapter Six

Summary

This thesis has investigated different optical and optomechanical systems based on whispering-gallery microcavities. An almost ideal design is developed for optical power transfer between two waveguides where efficiency is solely limited by intrinsic losses of the intermediate optical resonator. These intrinsic loss mechanisms are experimentally studied and differentiated by a powerful technique based on thermal nonlinearities of the microcavity material. Important information about the interaction between cavity surface and the ambient environment has been obtained through this study. Taking advantage of slow response time of thermal effects, a clever pump and probe technique is developed to unveil Kerr nonlinearities of the microcavity material in presence of dominant thermal effects. Kerr nonlinearity in microcavities is observed and measured for the first time at room temperatures. The technique also enables accurate measurements of thermal response times in microcavity structures. A journey is also embarked on in an almost untouched territory in the field of optical microcavities. A novel type of nonlinearity generated by mutual coupling of optical and mechanical modes of a microcavity structure is discovered and analyzed theoretically and experimentally. The ramifications of the optomechanical interaction and applications of the so-called “radiation-pressure-driven micromechanical oscillator” are discussed in diverse fields of science ranging from quantum mechanics to LIGO project to all-optical clocks on a chip.

Around The Rim: elegy to a photonic clock

PUMP POWER vibrates steadily, pumped
 80 million times per second
 when its rim probed
 steadily above threshold
 exceeds vibrations, saturates at high pump powers
 sensitive power detection
 exerts radiation pressure
 pressure in much the same way
 fully quench upon probe contact

the disk itself swells
 manipulated
 a probe-controlled
 micropositioner---insertion---loss
 communication fidelity

signal amplitude around the rim
 rim swells, inflated then deflates
 cycle repeats, repeats, repetition continues
 forcing function frequency
 pumped into
 into the disk, thermally actuated
 harmonics were observed
 shift in the whispering gallery

repetitive processes---cavities susceptible to these oscillations
 integrate interactions of motion

motion at a quantum level, entanglement proposed
 continuous flame hating
 up/down shifted and stretching
 an overall loaded factor
 high-finesse cavities
 loaded

sensitivity is boosted
 circuits integrated
 could be of help, coupling allows
 separation
 always exciting---stress field
 around the rim
 a mechanism to investigate such interactions
 a mechanism that needs to be understood better

Robin Diamond

